Tectonophysics 924 (2026) 231086

Contents lists available at ScienceDirect

Tectonophysics

journal homepage: www.elsevier.com/locate/tecto

Cenozoic cooling and exhumation history of Southern Ecuador: The role of plate-boundary reorganizations and inboard tectonic conditions

Leidy Carolina Sandoval-Espinel [a,b,c,*], Massimiliano Zattin [a], Mauricio A. Bermúdez [b], Cesar Witt [c], Jorge Iglesias [c], Maria Jose Hernández [d]

[a] University of Padova, Geosciences Department, Via Giovanni Gradenigo 6, 35131 Padova, Italy
[b] Pedagogical and Technological University of Colombia, School of Geological Engineering, 152211 Sogamoso, Colombia
[c] Univ. Lille, CNRS, IRD, Univ. Littoral Côte d'Opale, UMR 8187, LOG, Laboratoire d'Océanologie et de Géosciences, F 59000 Lille, France
[d] Departamento de Geología, Escuela Politécnica Nacional, Ladrón de Guevara E11 - 253, Quito, Ecuador

ARTICLE INFO

Keywords:
Exhumation
Cooling
Thermal-modeling
Structural inheritance
Plate convergence
Rock cooling
Southern Ecuador

ABSTRACT

The cooling and exhumation history of orogens along subduction systems provides unique constraints on regional tectonic evolution, reflecting the interplay between crustal deformation and plate convergence dynamics. Southern Ecuador lies within a transitional zone between the northern and central Andes, where contrasting tectonic histories have generated variations in inherited crustal architecture that influence how regional plate-boundary forcing is expressed in the upper plate. We present new apatite fission-track thermochronology data from seventeen plutonic rock samples across five crustal blocks in southern Ecuador: Western Cordillera, Eastern Cordillera, Intermontane basins, Celica-Lancones, and Amotape-Tahuin. Our results show that cooling ages are internally consistent within each block but differ across them, revealing a pattern of diachronous exhumation in most blocks. Some blocks instead record pronounced post-magmatic cooling, suggesting shallow pluton emplacement. Thermal history modeling, based on good-fit time–temperature paths indicates that regional exhumation initiated in the middle Eocene and persisted thereafter. The cooling trajectories group into three distinct, albeit partially overlapping, intervals: ~45–38 Ma (middle - late Eocene), ~40–30 Ma (late Eocene – early Oligocene), and ~ 33–25 Ma (Oligocene). We interpret this protracted and spatially variable exhumation as reflecting changes in the boundary conditions of the subduction system, including a transition from oblique to more orthogonal convergence and increases in convergence rates during the Cenozoic. However, the observed spatial variability is more directly linked to the progressive re-activation of major fault systems and, locally, to magmatic activity.

1. Introduction

The timing, drivers, and spatial expression of exhumation and topographic growth in the Andean mountain range remain intensively debated. Geological and thermochronology evidence demonstrates a long history of crustal deformation and exhumation since at least the Late Cretaceous (e.g., Bermúdez et al., 2019; Boschman, 2021; Noriega-Londoño et al., 2020; Restrepo-Moreno et al., 2019; Ronda et al., 2022; Sandoval-Espinel et al., 2024; Spikings et al., 2005; Zapata et al., 2019). At the same time, multiple lines of evidence, including provenance analysis, biostratigraphic constraints and paleoenvironmental records, suggest that the most significant phase of Andean topographic growth occurred during the Miocene (e.g., Anderson et al., 2016; Echeverri et al., 2015; Giambiagi et al., 2022; Howlett et al., 2025; Mosolf et al., 2011; Steinmann et al., 1999), when accelerated uplift and crustal shortening established the Andes as a major orographic barrier (Horton, 2018).

The timing and mechanisms of exhumation and uplift are not uniform along the orogen and remain poorly constrained in many regions, particularly in Ecuador. Here, exhumation has been primarily attributed to successive oceanic terrane-accretion events, including the incorporation of Caribbean-derived terranes (e.g., Ruiz et al., 2004; Spikings et al., 2001, 2005, 2010), as well as to the subduction of aseismic ridges such as the Carnegie Ridge (Brichau et al., 2021; George et al., 2022; Gutscher, 2002; Margirier et al., 2023; Michaud et al., 2009; Spikings et al., 2010). To a lesser extent, exhumation has also been linked to

* Corresponding author at: University of Padova, Geosciences Department, Via Giovanni Gradenigo 6, 35131 Padova, Italy.
E-mail address: leidycarolina.sandovalespinel@studenti.unipd.it (L.C. Sandoval-Espinel).

https://doi.org/10.1016/j.tecto.2026.231086
Received 22 August 2025; Received in revised form 12 January 2026; Accepted 14 January 2026
Available online 16 January 2026

changes in subduction dynamics, including variations in convergence rates (Margirier et al., 2023; Spikings et al., 2005, 2010) and shifts in the subduction vector toward more orthogonal convergence (Jaillard, 2025).

Most thermochronological studies in Ecuador have focused on the northern segment of the margin (e.g., Brichau et al., 2021; Margirier et al., 2023; Ruiz et al., 2004; Spikings et al., 2000, 2005, 2010), particularly between ~1°N and 2°S, where the Carnegie Ridge is currently subducting (Gutscher et al., 2000; Michaud et al., 2009). In contrast, southern Ecuador remains comparatively under-studied, with existing data largely limited to the Western and Eastern Cordilleras and the Amotape–Tahuin Block (ATB; Margirier et al., 2023; Spikings et al., 2001, 2005, 2010). Other structural blocks, including the Celica–Lancones Basin, the Intermontane basins, and the Inter-Andean Valley, have received little to no thermochronological attention (e.g., Espurt et al., 2018; Steinmann et al., 1999).

Southern Ecuador offers a strategic location to determine whether exhumation arises from terrane-accretion processes, shifts in subduction dynamics, or a combination of both. This region lies south of the Colombian–north central Ecuadorian margin, where accretionary events were pronounced (Restrepo-Moreno et al., 2019; Ruiz et al., 2004; Spikings et al., 2000).

In this study, we present seventeen new AFT ages from bedrock samples from across southern Ecuador (Fig. 1B), spanning major crustal blocks including the Celica-Lancones Arc, the Western and Eastern Cordilleras, the ATB, and several Cenozoic intrusives intruding the Intermontane basins. Using thermal history modeling, we assess the timing and rates of exhumation and investigate spatial variations across strike. Our results indicate a protracted exhumation history punctuated by three cooling intervals. These intervals broadly correlate with changes in subduction dynamics, including transitions from oblique to more orthogonal convergence and increases in convergence rates. However, the distinct timings and rates of cooling between adjacent crustal blocks suggest that deformation was primarily accommodated along major crustal faults.

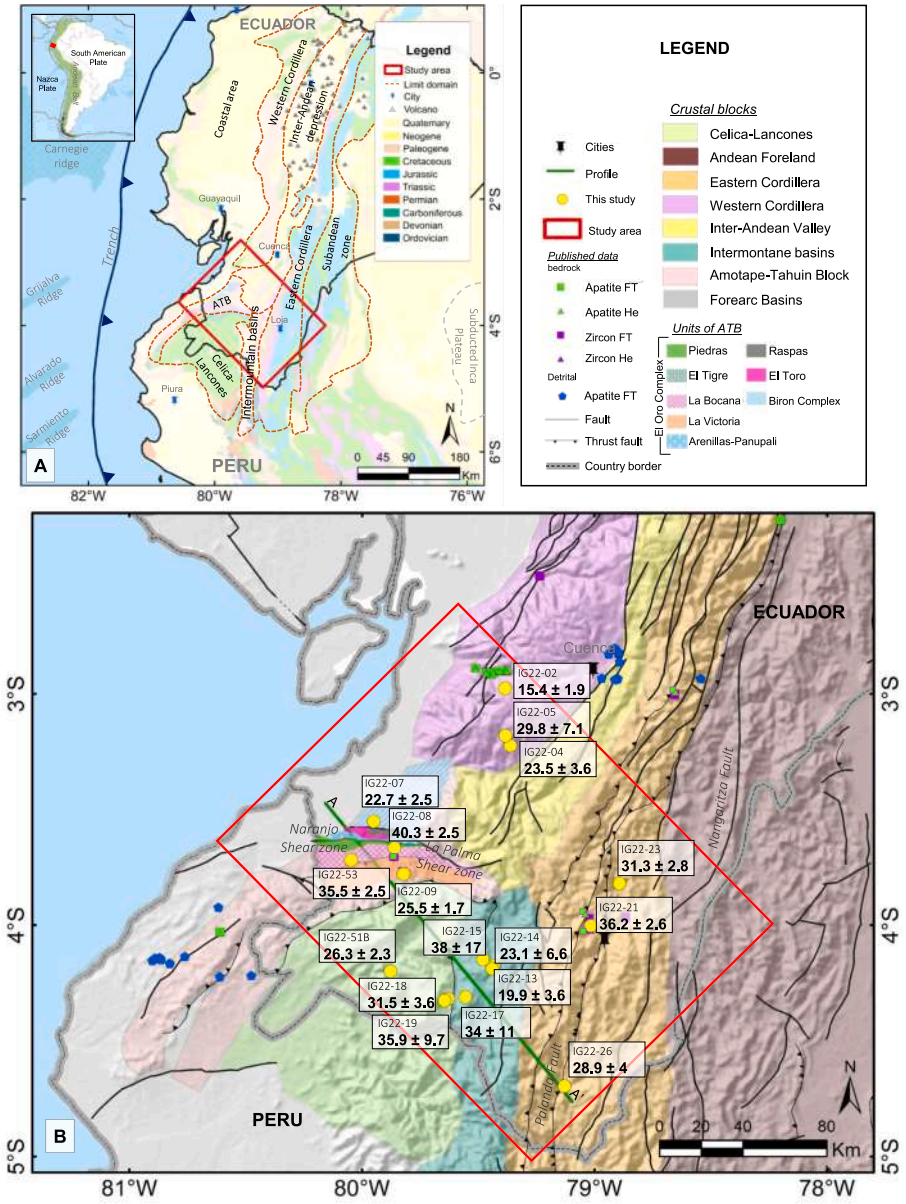

Fig. 1. (A) Regional geology of central-southern Ecuador, highlighting major faults. (B) Sketch map of southern Ecuador showing crustal blocks and sample locations analyzed in this study, along with published thermochronological data (ZFT, AFT, AHe, and ZHe) from Spikings et al. (2001, 2005, 2010); Espurt et al. (2018); Steinmann et al. (1999); and Margirier et al. (2023). ATB: Amotape-Tahuin block.

2. Geological background and previous thermochronological studies

2.1. Geological overview

The Ecuadorian Andes represent a composite orogenic belt characterized as a bivergent orogen, with active thrusting along the western flank of the Western Cordillera and the sub-Andean ranges to the east (Fig. 1; Baby et al., 2013; Eguez et al., 2003; Hernández et al., 2024; Jaillard et al., 2005). This orogeny has evolved through a complex history of subduction processes, involving Mesozoic-Cenozoic accretionary events (Aizprua et al., 2019; Hughes and Pilatasig, 2002; Jaillard, 2022; Kerr and Tarney, 2005; Reynaud et al., 1999; Vallejo et al., 2006; Witt et al., 2019), transitions between compressional and extensional settings (George et al., 2021; Witt et al., 2023) and variations in convergence rates (Maloney et al., 2013).

This intricate tectonic evolution has given rise to a number of distinct crustal blocks throughout southern Ecuador (Fig. 1A). Each region reflects a different geological history and lithological composition. To the east lies the Eastern Cordillera, also known as the Cordillera Real, which comprises Paleozoic to Lower Cretaceous metamorphic rocks (Kennan, 2000; Litherland, 1994). To the west of this range lies the Inter-Andean Valley, a structural depression filled with Cenozoic volcanic and sedimentary rocks (e.g., Hungerbühler et al., 2002). Adjacent to the west are the Intermontane basins, which were accompanied by sustained magmatic activity until ~5 Ma (e.g., Schütte et al., 2010). Further west lies the Cretaceous Celica-Lancones Basin, whose eastern segment is dominated by continental Late Cretaceous arc-related igneous rocks and volcaniclastic deposits (e.g., The Alamor and Celica Fms; Jaillard et al., 1996; Reynaud et al., 1996; Valarezo et al., 2019), while the central-western part is mainly composed of siliciclastic deposits (Jaillard et al., 1999; Winter et al., 2010; and references therein). Farther west lies the ATB (Fig. 1B), an *E*-W trending low elevation range that shifts to a NE-SW orientation in Peru (Mourier, 1988; Witt et al., 2017). It can be subdivided into two main domains: the El Oro Complex, located south of the Naranjo Shear Zone (NSZ), which includes the Las Piedras Unit and the Tahuin Group (Noble et al., 1997; Riel et al., 2014), and a regional-scale mélange zone north of the NSZ, containing high-pressure rocks primarily from the Raspas Ophiolitic Complex and the Biron Complex (Riel et al., 2014).

2.2. Previous thermochronological studies

Published thermochronological data from southern Ecuador (Table S1; Fig. 1B) are concentrated in the Western and Eastern Cordilleras and the ATB. These studies document three principal cooling phases at ~75–55 Ma (ZFT and AFT; Spikings et al., 2001, 2005), ~43–30 Ma (ZFT, AFT, and AHe; Spikings et al., 2010), and ~ 20–5 Ma (AFT, AHe; Margirier et al., 2023; Spikings et al., 2001, 2010), each linked to major tectonic and geodynamic events.

The ~75–55 Ma cooling phase in south Ecuador has been tentatively linked to the collision and accretion of the Pallatanga terrane in north-central Ecuador (e.g., Spikings et al., 2001, 2005, 2010) or to increment in convergence rates (see Espurt et al., 2018). The ~43–30 Ma interval was initially attributed to the collision of the Macuchi intra-oceanic arc with the Pallatanga Terrane (e.g., Spikings et al., 2001, 2005), but, more recently, this event has been linked exclusively to changes in plate kinematics (accelerated subduction rates; Espurt et al., 2018; Spikings et al., 2010). Cooling during the ~20–5 Ma interval has been widely associated with the onset of Carnegie Ridge subduction. For example, Spikings et al. (2000, 2001) proposed an early onset of Carnegie Ridge subduction at ~15–10 Ma based on the exhumation history of the Eastern Cordillera. In contrast, studies conducted in the Western Cordillera suggest a later onset of about 6–5 Ma (e.g., Margirier et al., 2023).

3. Sampling and methods

We collected seventeen bedrock samples from the Eastern Cordillera, the Western Cordillera, the Intermontane basins, the Celica-Lancones arc, and the ATB. Their locations and key details are provided in Table 1 and illustrated in Fig. 1B.

3.1. Apatite fission-track thermochronology

Apatite fission track thermochronology is based on the defects produced by the spontaneous fission of ^{238}U (Gleadow, 1981), which can be retained, or annealed depending on the temperature. Thus, this method can be used to reconstruct the thermal history of rocks by providing insights into their cooling within the shallow crust (e.g., Armstrong et al., 2003; Gallagher et al., 1998; Gleadow et al., 2002). The temperature range in which fission tracks partially anneal is referred to as the partial annealing zone (PAZ), and is typically used to record the cooling of rocks within the 60 °C to 120 °C interval (Gallagher et al., 1998).

Sample preparation took place at the Pedagogical and Technological University of Colombia (UPTC). Samples were crushed, sieved, and separated using hydro-gravimetric and magnetic methods (Frantz magnetic separator with current increments from 0.2 to 1.2 Amperes) to isolate the heavy and non-magnetic fractions. Subsequently, gravimetric separation was carried out using standard heavy liquids (bromoform: ~2.89 g/cm^3 and diiodomethane: ~3.32 g/cm^3) to concentrate apatite fraction.

Apatite mounts were prepared using the external detector method (EDM), which utilizes a Zeta calibration factor (Hurford and Green, 1983). This factor was determined by analyzing the Fish Canyon and Durango age standards at the Thermochronology Laboratory of the University of Padova, Italy. Crystals were selected using an Olympus SZX16 binocular microscope, mounted on double-sided tape, embedded in epoxy sheets, and polished to expose their internal surfaces. The exposed surfaces were then etched with a solution 5 N of nitric acid HNO_3 during for 20 s at 20 °C to etch fission tracks. The mountings were covered with mica detectors and irradiated in two separate campaigns (OSU28, OSU29B) at the Oregon State Radiation Center, USA, with nominal fluence between 6×10^{-17} a^{-1} to 9×10^{-17} a^{-1}. The irradiation tubes included Fish Canyon, Mount Dromedary, and Durango age standards, as well as CN5 dosimeter glasses. After irradiation, the mica detectors were detached, etched with 40 % HF at 20 °C for 45 min, and prepared for track counting.

Fission tracks were counted dry at 1250× magnification using an Olympus BX-51 optical microscope with an automated XY-stage system at the University of Padova. Ages were calculated using a zeta value of 356.04 ± 14.58 (zeta determined by analyst Sandoval Leidy C. for the CN5 dosimeter glass). Under the same system, etch pit diameters (Dpar) were measured, and where possible confined fission tracks lengths were obtained. AFT ages are reported as central ages with 1σ standard deviations, calculated using the radial plot software developed by Vermeesch (2018). Detailed AFT results are summarized in Table 2, with associated radial plots shown in Fig. 2.

3.2. Thermal modeling

Thermal histories were reconstructed using the HeFTy software version 2.1.7 developed by Ketcham (2005), which employs a 'Frequentist' approach that uses formal statistical hypothesis tests to assess the goodness-of-fit between the input data and the thermal model predictions. We applied the annealing model of Ketcham et al. (2007), used etch pit diameters (Dpar) as kinetic parameters (Donelick et al., 2005), and aimed to minimize constraints in the model to avoid over-constraining.

To guide the thermal history modeling, we defined two primary constraint boxes for all samples. These constraints reduce model ambiguity by integrating independent geological and geochronological

Table 1
Sample locations and zircon U-Pb ages.

Sample Name	Lat. (S)	Long. (W)	Elevation (m)	U-Pb age (Ma)	± 1σ (Ma)	Rock Type	Crustal block	Source
IG22–02	2.9769	79.3842	3480.3	13.3	0.2	Granodiorite	Western Cordillera	Iglesias et al. (2025)
IG22–04	3.2238	79.3621	2246.37	29.7	2	Quartz-diorite	Western Cordillera	Iglesias et al. (2025)
IG22–05	3.1809	79.3824	2716.3	1035.7*	5.1	Granodiorite	Western Cordillera	Iglesias et al. (2025)
IG22–07	3.5515	79.9495	72.58	NA	NA	Plutonic	ATB (Biron complex)	This study
IG22–08	3.6657	79.8601	226.14	NA	NA	Granodiorite	ATB (El Oro Complex)	This study
IG22–09	3.7678	79.8249	749.56	200–1000		Metaquartzite	ATB (El Oro Complex)	Sandoval-Espinel et al. (2025)
IG22–13	4.1758	79.4336	2024.37	18.5	0.2	Quartz-diorite	Intermontane basins	Iglesias et al. (2025)
IG22–14	4.1891	79.4395	2133.67	21.7	0.4	Tonalite	Intermontane basins	Iglesias et al. (2025)
IG22–15	4.1486	79.4793	1427.23	36.7	0.4	Tonalite	Intermontane basins	Iglesias et al. (2025)
IG22–17	4.3109	79.5552	1906.31	NA	NA	Plutonic	Intermontane basins	This study
IG22–18	4.3310	79.6262	1880.65	96.3	2.1	Gabbro	Celica-Lancones arc	Sandoval Espinel et al. (2026)
IG22–19	4.3260	79.5844	1965.76	94.7	0.9	Granodiorite	Celica-Lancones arc	Sandoval Espinel et al. (2026)
IG22–21	4.0027	79.0148	1546.22	NA	NA	Granodiorite	Eastern Cordillera (Sabanilla)	Sandoval Espinel et al. (2026)
IG22–23	3.8204	78.8921	874.21	191.6	1.8	Granodiorite	Eastern Cordillera (Zamora)	Sandoval Espinel et al. (2026)
IG22–26	4.6966	79.1287	1042.43	179.2	1.1	Granodiorite	Eastern Cordillera (Zamora)	Sandoval Espinel et al. (2026)
IG22-51B	4.1992	79.8767	549.1	100.8	1.8	Diorite	Celica-Lancones arc	Sandoval Espinel et al. (2026)
IG22–53	3.7183	80.0464	521.3	235.5	3.7	Granite	ATB (El Oro Complex)	Sandoval Espinel et al. (2026)

NA: not available. *: Inherited component, no crystallization age is available.

Table 2
AFT data from southern Ecuador.

Sample	Crustal block	nG	ρd (10^6 /cm^2)	∑Ns	∑Ni	P(χ2) (%)	Central Age (Ma)	± 1σ (Ma)	nL	MTL	± 1σ (μm)	Dpar (μm)
IG22–02	Western Cordillera	20	1.206	75	1004	100	15.4	1.9	29	14.18	1.18	2.90
IG22–05	Western Cordillera	8	1.199	21	150	100	29.8	7.1	24	13.43	1.51	2.30
IG22–04	Western Cordillera	19	1.192	55	495	100	23.5	3.6	22	13.71	1.64	2.20
IG22–07	ATB (Biron complex)	20	1.178	166	1278	100	27.2	2.5	30	13.70	1.70	2.00
IG22–08	ATB (El Oro Complex)	20	1.171	521	2689	90	40.3	2.5	72	13.23	1.05	1.80
IG22–09	ATB (El Oro Complex)	20	1.164	368	2988	100	25.5	1.8	36	13.71	1.43	2.30
IG22–13	Intermontane basins	20	1.157	33	341	100	19.9	3.6	30	13.82	1.20	2.02
IG22–14	Intermontane basins	10	1.240	16	129	100	23.1	6.6	24	13.06	0.80	3.00
IG22–15	Intermontane basins	3	1.233	6	35	75	38.0	17	0	–	–	2.10
IG22–17	Intermontane basins	5	1.225	11	71	90	34.0	11	0	–	–	1.95
IG22–18	Celica-Lancones arc	19	1.150	110	713	100	31.5	3.6	14	14.15	1.09	2.80
IG22–19	Celica-Lancones arc	13	1.218	16	97	100	35.9	9.7	31	13.37	0.92	2.20
IG22–21	Eastern Cordillera (Sabanilla)	20	1.210	331	1966	91	36.2	2.6	71	13.10	1.60	2.80
IG22–23	Eastern Cordillera (Zamora)	20	1.203	178	1214	100	31.3	2.8	11	13.89	0.75	2.80
IG22–26	Eastern Cordillera (Zamora)	11	1.123	66	456	100	28.9	4.0	21	12.94	1.43	1.90
IG22-51B	Celica-Lancones arc	20	1.019	187	1283	98	26.3	2.3	37	12.89	1.4	2.12
IG22–53	ATB (El Oro Complex)	20	1.012	432	2185	83	35.5	2.4	33	13.3	1.4	1.81

nG: number of grains. Ns: Spontaneous tracks. Ni: Induced tracks. nL: number of confined fission-tracks. MTL: mean track length. P(χ2) = Chi-square probability that the single grain ages represent one population; MTL = mean track length; Dpar = Etch-pit width parallel to the C-axis (Barbarand et al., 2003; Carlson et al., 1999); SD = standard deviation of track-length distribution and etch-pit width measurements, respectively.

evidence. The first constraint was based on U-Pb zircon crystallization ages from the same samples (Iglesias et al., 2025; Sandoval Espinel et al., 2026). The second constraint represents the present-day surface temperature, fixed at 20 ± 5 °C.

For samples from the ATB (samples IG22–53, IG22–07, IG22–08, and IG22–09), we applied an additional constraint derived from stratigraphic and structural evidence indicating that the massif was exposed at the surface during the Late Cretaceous (Albian–Maastrichtian) and was unconformably overlaid by the continental fluvial environments to shallow marine Puyango–Cazaderos and Cochurco formations (Jaillard et al., 1999; Riel et al., 2014).

For samples from the Western Cordillera (IG22–21 and IG22–23), we incorporated previously published AHe data (weighted average age and uncertainty) from Spikings et al. (2010) into the thermal models to improve temporal constraints on the cooling histories. For sample IG22–21, AHe data from samples 99RS40 (43.6 ± 06 Ma) and 99RS41 (38.3 ± 1 Ma; Table S1), located within ~5 km of our sampling site, were included. For sample IG22–23, AHe data from sample 99RS43, located within ~15 km, were incorporated. The inclusion of these nearby samples is justified by their position within the same structural block and their consistent lithological context, supporting the assumption that they experienced a similar thermal history.

Models were run until 500 good paths (defined as those that statistically fit the observed AFT ages and length distributions within the imposed constraints, *p*-value ≥0.05, and GOF of ~1.0) were found. Samples IG22–15 and IG22–17 were excluded due to having too few grains (fewer than 5) and no measured confined track lengths. Time-temperature models are shown in Figs. 3 and S1, and their corresponding mean track length (MTL) distributions for both measured and modeled data are shown in Fig. S1.

Finally, to estimate exhumation rates, we used the Age2EDOT program (Brandon et al., 1998; Ehlers et al., 2005), which models cooling rates and calculates the apparent geothermal gradient (dT/dZ, °C/km) for a given thermochronometric system. As input parameters we assumed a surface temperature of 20 °C and a geothermal gradient of 35 °C/km, consistent with the elevated heat flow observed in the present-day southern Ecuadorian magmatic arc. Given the long-lived magmatic activity in this region and the absence of evidence for significant thermal regime changes, it is reasonable to infer that past geothermal gradient were comparable to current values, which typically exceed 30 °C/km (e.g., Angulo-Romero et al., 2023).

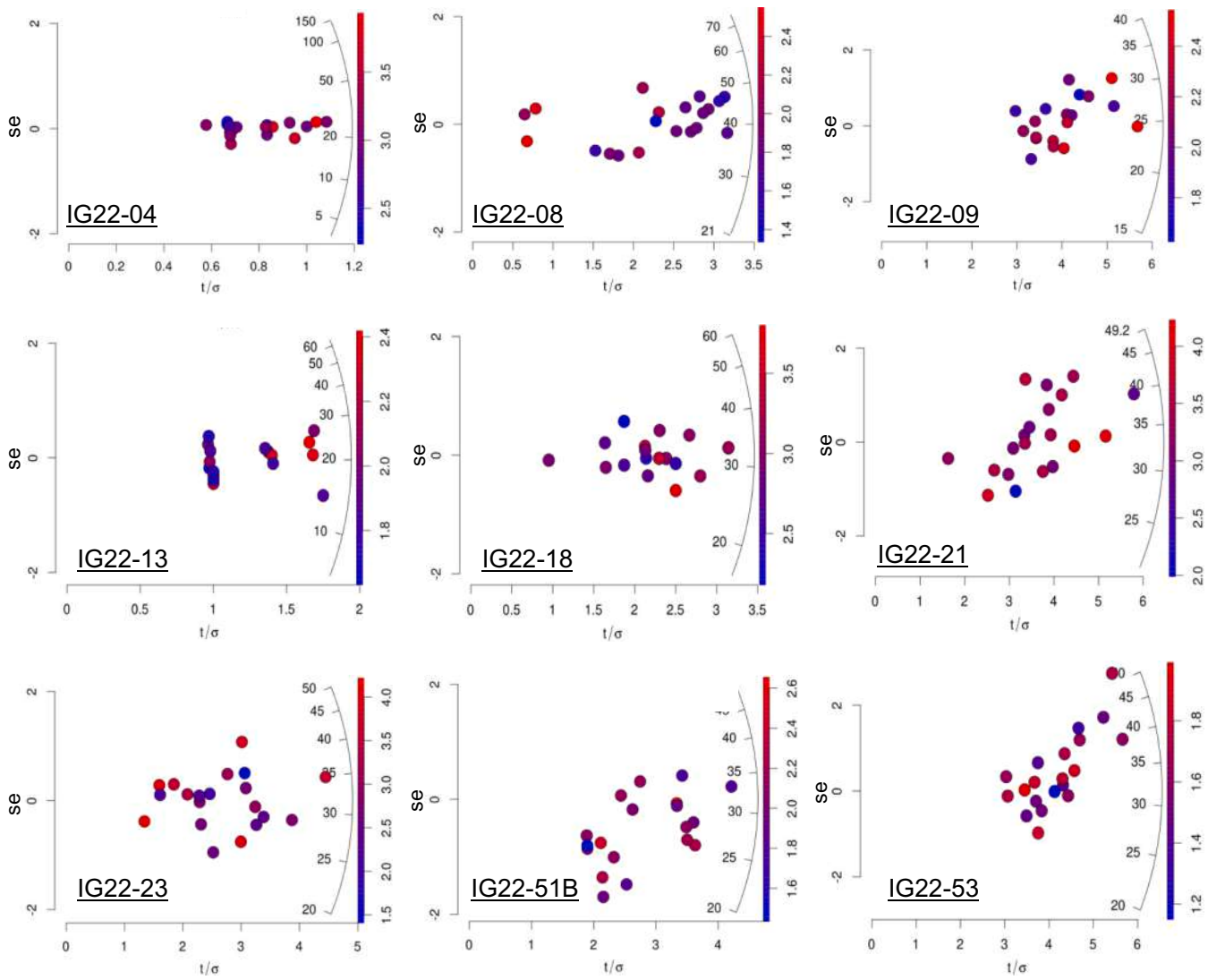

Fig. 2. Radial plots of apatite fission track (AFT) data for selected samples from this study, illustrating single-grain age distributions. The color bar to the right of each plot indicates Dpar values (in μm), with bluish hues denoting smaller etch pit diameters and reddish hues indicating larger Dpar values.

4. Results and interpretation

4.1. AFT thermochronology

AFT ages range from 40.3 ± 2.5 Ma (sample IG22–08; Fig. 2) to 15.4 ± 1.9 Ma (sample IG22–02). In general, samples from the Celica–Lancones Arc and the Eastern Cordillera show a positive correlation between age and elevation (Fig. 4A and E), while samples from the ATB display a negative correlation. In the Western Cordillera, the three samples form a boomerang pattern with no clear age–elevation relationship. MTL range from 12.89 μm to 14.18 μm (Fig. 4B), and Dpar values range from 1.8 μm to 3.0 μm (Fig. 4C). All samples passed the p (χ^2) test, indicating the presence of a single population.

Four AFT ages were obtained from the ATB (Fig. 1B), including three samples from the El Oro Complex. The Triassic granite (IG22–53) yielded an AFT age of 35.5 ± 2.4 Ma and a MTL of 13.3 ± 1.4 μm. The granodiorite (IG22–08) gave an age of 40.3 ± 2.5 Ma and an MTL of 13.2 ± 1.1 μm, whereas the granite (IG22–09) yielded 25.5 ± 1.8 Ma and an MTL of 13.7 ± 1.4 μm. The northernmost sample (IG22–07), from the Biron Complex, yielded an age of 27.2 ± 2.5 Ma with an MTL of 13.7 ± 1.7 μm. These results indicate protracted cooling of the ATB from the late Eocene to early Miocene.

Three plutonic samples from the Western Cordillera were analyzed (Fig. 1B). The Oligocene quartz-diorite (IG22–04) gave an AFT age of 23.5 ± 3.6 Ma and an MTL of 13.7 ± 1.6 μm, while sample IG22–05 yielded an AFT age of 29.8 ± 7.1 Ma with an MTL of 13.4 ± 1.5 μm. The Miocene granodiorite IG22–02 yielded an AFT age of 15.4 ± 1.9 Ma and an MTL of 14.2 ± 1.2 μm; this age closely matches its zircon U-Pb crystallization age of 13.3 ± 0.2 Ma (Table 1), indicating rapid post-magmatic cooling.

Three Late Cretaceous samples from the Celica–Lancones Arc (gabbro IG22–18, granodiorite IG22–19, diorite IG22-51B; Fig. 1B) yielded AFT ages ranging from 35.9 ± 9.7 Ma to 26.3 ± 2.3 Ma, with MTL values between 13.3 ± 1.4 μm and 14.1 ± 1.5 μm. Additionally, sample IG22–19, despite having 13 counted apatite grains (typically sufficient for igneous rocks; Table 2), exhibits an unusually large age uncertainty, likely related to variable track preservation, heterogeneous uranium distribution, or analytical limitations.

Four granitoids samples from the Intermontane Basins (IG22–13, IG22–14, IG22–15, IG22–17; Fig. 1B) yielded AFT ages between 19.9 ± 3.6 Ma and 38 ± 11 Ma; these overlap with their respective zircon U-Pb crystallization ages (Iglesias et al., 2025), suggesting mainly post-magmatic cooling.

Three granodiorite samples from the Eastern Cordillera yielded Oligocene to Eocene AFT ages. Samples IG22–26 and IG22–23, located east of the Palanda Fault (Fig. 1), yielded similar Oligocene ages of 28.9

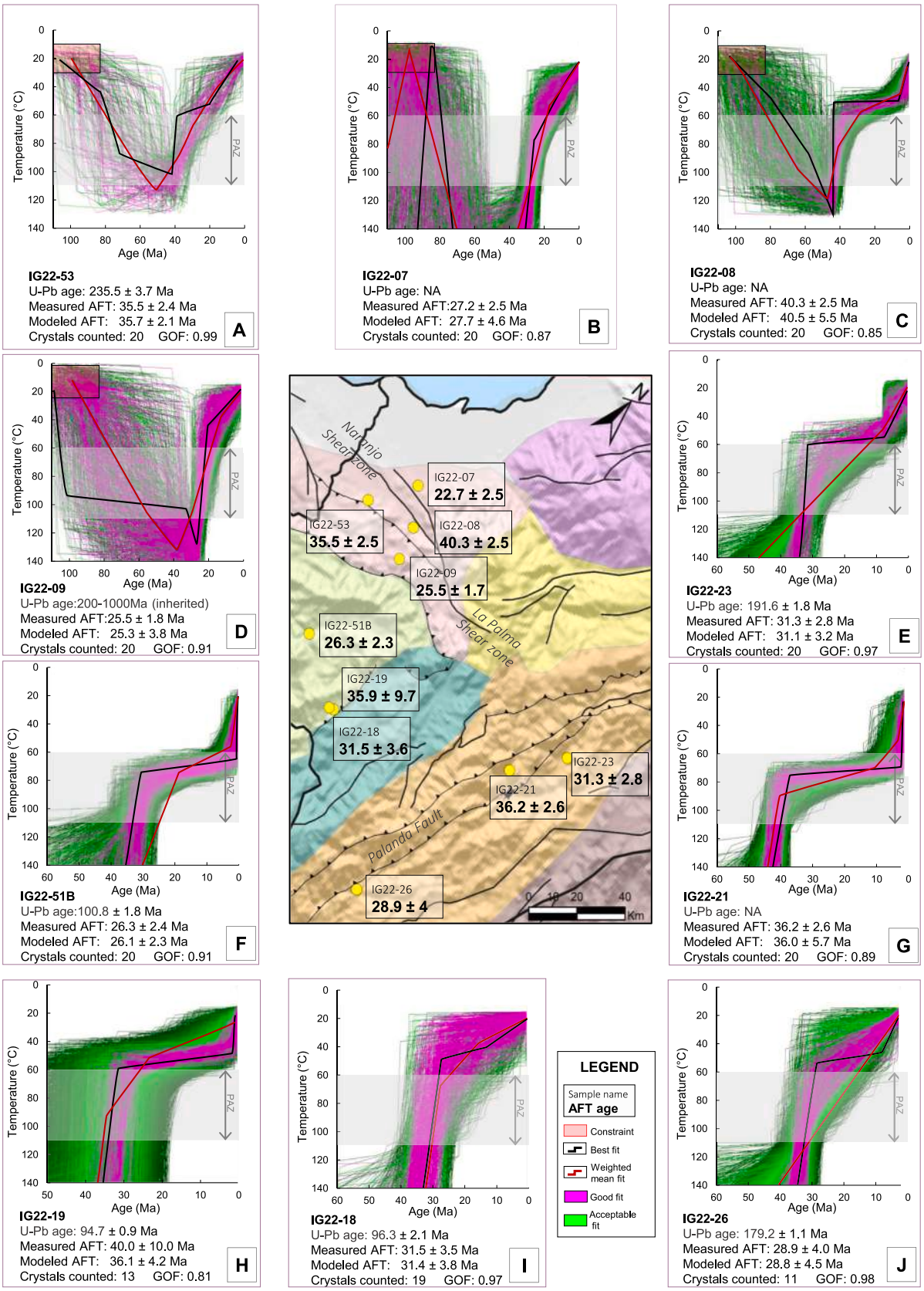

Fig. 3. Map showing the location of the samples analyzed in this study, with color coding consistent with Fig. 1. For each sample that records exhumation-related cooling, the corresponding time-temperature (T–t) histories modeled using HeFTy (Ketcham, 2005) is shown. Model constraints are included (see text for details); however, U-Pb crystallization age constraints are not displayed, as they fall outside the plotted time range. The black lines represent the best-fit thermal history, and the red lines show the weighted mean fit. PAZ: partial annealing zone. (For interpretation of the references to color in this figure legend, the reader is referred to the web version of this article.)

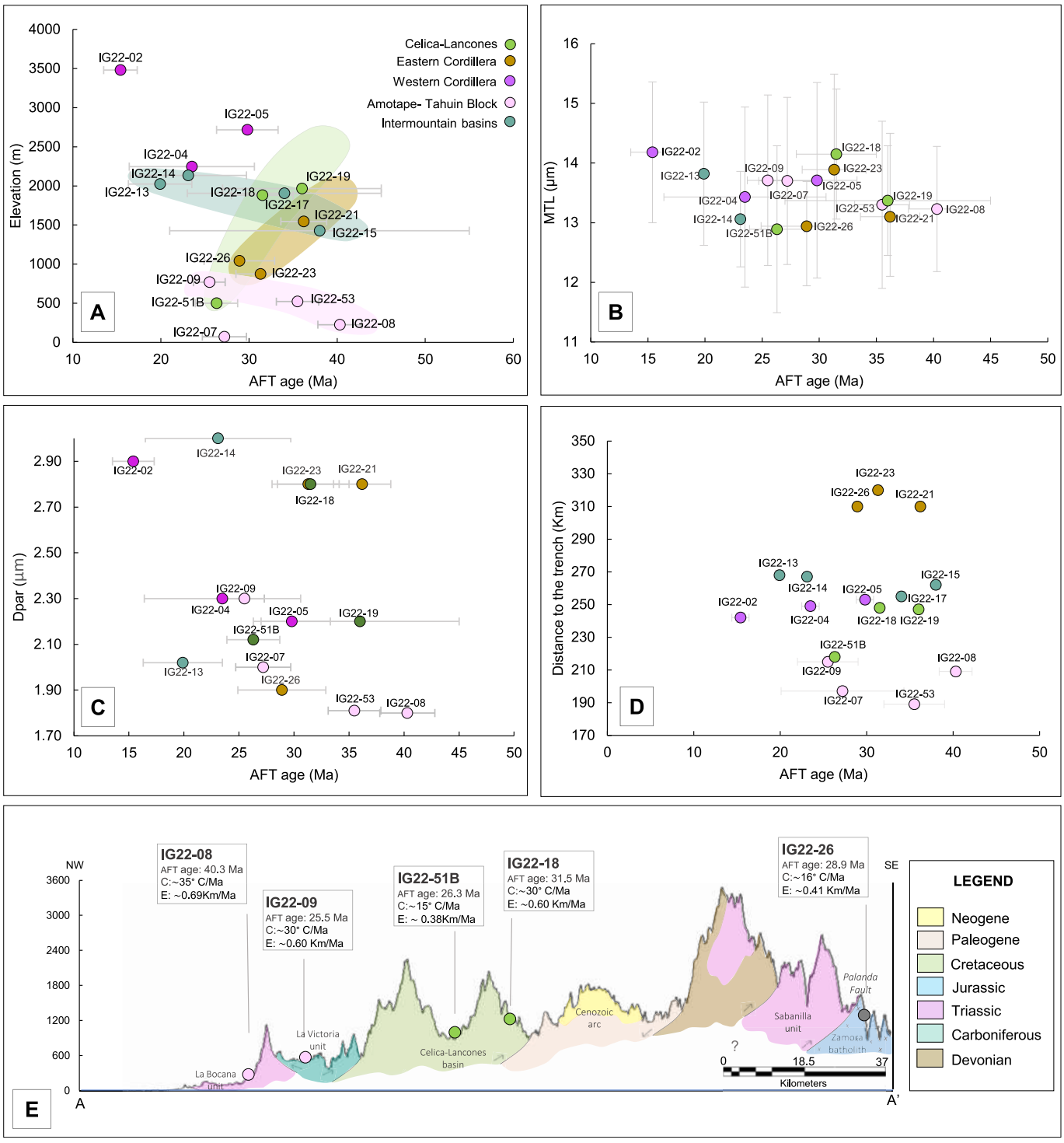

Fig. 4. (A) Age-elevation relationships, (B) Mean track length (MTL) vs. AFT age, (C) Dpar vs. AFT age, and (D) Distance to the trench vs. age (E) Topographic profile illustrating sample locations. The locations of the profiles are shown in Fig. 1C. C: cooling rate. E: exhumation rate.

± 4.0 Ma and 31.3 ± 2.8 Ma, respectively, whereas sample IG22–21, west of the fault, present an older Eocene age of 36.2 ± 2.6 Ma. These differences may reflect differential exhumation across the Palanda Fault during the late Eocene to Oligocene.

4.2. Thermal history models

A) Amotape-Tahuín Block (ATB)

Samples IG22–53 (Fig. 3A) and IG22–08 (Fig. 3C) record similar thermal histories. Both samples were exhumed and served as sediment sources for Albian–Maastrichtian sedimentary formations (Jaillard et al., 1999; Riel et al., 2014). Following burial and reheating, they experienced cooling between ~45 and 40 Ma. Although some good-fit paths show thermal quiescence between ~60 and 40 Ma. The best-fit models indicate rapid 42–40 Ma cooling at ~35 °C/Ma, corresponding to exhumation of ~0.7 km/Ma considering a geothermal gradient of 35 °C/km.

In contrast, the northernmost (IG22–07; Fig. 3B) and southernmost (IG22–09; Fig. 3D) samples record reheating followed by later cooling, at ~33–25 Ma. Their best-fit models yield rates of ~30–35 °C/Ma (equivalent to ~0.6–0.7 km/Ma of exhumation). Mean track lengths >13 μm (Fig. 4B, Table 2) across the ATB indicate short residence times within the partial annealing zone, consistent with relatively rapid exhumation.

B) Celica-Lancones arc

Samples from this block (IG22-51B, IG22–19, and IG22–18; Fig. 3F, H, and I, respectively) show cooling primarily between ~40 and 29 Ma, as indicated by the majority of good-fit paths, with only a few paths suggesting cooling in the ~50–40 Ma interval. Best-fit models for all samples indicate cooling initiated at ~35–33 Ma, at rates of ~15–30 °C/Ma, equivalent to exhumation of ~0.4–0.6 km/Ma.

C) Eastern Cordillera

Samples IG22–23 and IG22–26, located east of the Palanda Fault (Figs. 1 and 3), exhibit broadly similar thermal histories. Sample IG22–23 (Fig. 3E) shows cooling mainly between ~38 and 32 Ma, as indicated by most of the good-fit paths. Sample IG22–26 (Fig. 3J) records a similar primary cooling interval, although a few paths extend to around 42 Ma. The best-fit models for these samples indicate cooling between ~34 and 32 Ma, with rates of about 16–20 °C/Ma,

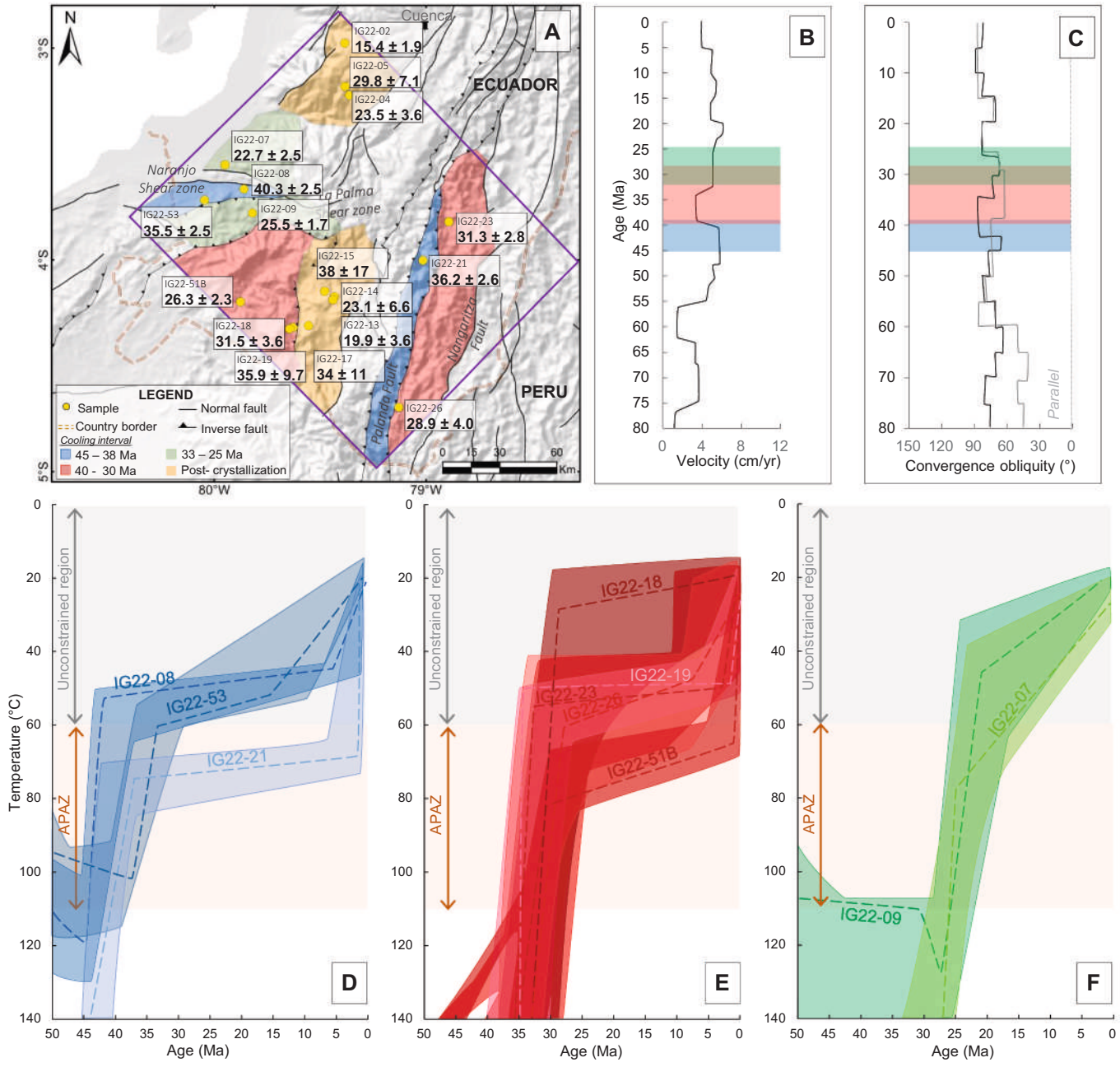

Fig. 5. (A) Map of the study area showing crustal blocks color-coded according to their corresponding cooling intervals. (B) Normal convergence rates over time for the Nazca Plate (formerly Farallón) and the South American Plate, from Maloney et al. (2013). (C) Convergence obliquity versus age, after Jaillard (2025). (D-F) Summary of all good T–t paths identified in this study (shaded areas); dashed lines represent best-fit paths for individual samples. Shaded areas correspond to distinct cooling intervals: blue (45–38 Ma), red (40–30 Ma), and green (33–25 Ma). APAZ = apatite partial annealing zone. (For interpretation of the references to color in this figure legend, the reader is referred to the web version of this article.)

corresponding to exhumation rates of 0.4–0.5 km/Ma. In contrast, sample IG22–21, located west of the Palanda Fault, records an older cooling episode. All good-fit paths (Fig. 3G) indicate cooling between ca. 45 and 40 Ma, while the best-fit model suggests cooling at around 42 Ma, with a rate of about 20 °C/Ma, corresponding to an exhumation rate of ~0.5 km/Ma. A potential change in cooling rate is suggested by best-fit paths of all studied samples at temperatures lower than ~60 °C; however, this occurs out of the sensitivity range of the method employed in this study and cannot be evaluated further due to the absence of AHe data.

5. Discussion

5.1. Cooling events within the crustal blocks

The interpretation of regional exhumation patterns must be considered in light of sampling density. Although each major crustal block is represented, only 1–2 samples per block yielded suitable apatite concentrates, as many collected rocks contained apatites that were highly fractured, inclusion-rich, or otherwise unsuitable for reliable track counting. This limits high-resolution assessment of intra-block variability; however, the dataset still constitutes one of the most comprehensive AFT compilations for southern Ecuador and provides a robust first-order framework for reconstructing the region's cooling history. Our thermochronological dataset indicates broadly continuous and asynchronous exhumation across southern Ecuador (Fig. 5A), with cooling occurring in partially overlapping intervals across different crustal blocks (Figs. 3 and 5). Within this long-term exhumation history, three main cooling clusters can be recognized: (i) a middle- late Eocene interval (~45–38 Ma; Fig. 5D) characterized by rapid cooling of ~20–35 °C/Ma; (ii) a late Eocene– early Oligocene interval (~40–30 Ma; Fig. 5E) with cooling rates of ~15–30 °C/Ma; and (iii) Oligocene interval (~33–25 Ma; Fig. 5F), during which cooling rates increased again to ~30–35 °C/Ma. Beyond the exhumation-related cooling patterns, rapid post-magmatic cooling is also recorded in some structural blocks (Fig. 5A).

A) Eastern Cordillera

Cooling in the southern Eastern Cordillera was evaluated in two units: the Jurassic Zamora Batholith and the Triassic Sabanilla Unit. The Zamora Batholith, located east of the Palanda Fault (Figs. 1B and 3), records a cooling interval between ~38 and 32 Ma, with best-fit thermal models for samples IG22–23 and IG22–26 indicating rates of ~16–23 °C/Ma (Fig. 3E and J). Within the same structural block, Spikings et al. (2001) reported an AFT age of 34 ± 3.3 Ma and MTL of 12.6 ± 0.5 μm for sample 99RS43, which is consistent with our results, although they inferred slower cooling rates (10 °C/Ma). Farther east within the same batholith, along the Sub-Andean zone, the same authors documented older AFT ages between 61 and 59 Ma, suggesting an earlier phase of exhumation in that region. To the west of the Palanda Fault, the Sabanilla Unit experienced cooling between 45 and 40 Ma at a rate of ~20 °C/Ma (sample IG22–21; Fig. 3G). This event is consistent with the 45–30 Ma cooling phase at ~20 °C/Ma reported by Spikings et al. (2010) for the same unit. These results reveal distinct cooling histories across the Palanda fault, indicating that differential exhumation within the Eastern Cordillera. The findings also suggest that exhumation in the Eastern Cordillera began as early as the Paleocene and continued through the late Eocene–early Oligocene.

B) Intermontane basins

In the Intermontane region of southern Ecuador, igneous rocks represented by samples IG22–13 (AFT age: 19.9 ± 3.6 Ma; U-Pb age: 18.5 ± 0.2 Ma), IG22–14 (AFT age: 23.1 ± 6.6 Ma; U-Pb age: 21.7 ± 0.4 Ma), and IG22–15 (AFT age: 38.0 ± 17 Ma; U-Pb age: 36.7 ± 0.4 Ma) exhibit AFT and U-Pb ages that are broadly similar. This close correspondence indicates rapid post-crystallization cooling (Figs. 5A and 6), suggesting that these granitoids were emplaced at shallow crustal levels, likely near the PAZ. Therefore, the AFT ages likely record thermal relaxation following magmatic emplacement rather than significant exhumation (e.g., Malusà and Fitzgerald, 2019). However, coeval tectonically controlled exhumation cannot be completely ruled out, particularly in the context of ongoing convergence (Jaillard, 2025; and references therein), significant crustal thickening and exhumation recorded along the Northern Andes during the Miocene (e.g., Bermúdez et al., 2011; Horton et al., 2020; Margirier et al., 2023; Mora et al., 2010; Sandoval-Espinel et al., 2024; Spikings et al., 2000; Spikings et al., 2001). Throughout this period, some segments of the Northern Andes experienced the complete emergence of topographic features, leading to the establishment of the Andean belt as an effective orographic barrier (e.g., Horton et al., 2020; Witt et al., 2017).

C) Celica-Lancones arc

The Cenomanian rocks of the Celica-Lancones arc, located between the Intermontane basins to the east and the ATB to the west (Fig. 1), underwent synchronous cooling and exhumation between ~40 and 29 Ma, at estimated rates of ~15–20 °C/Ma. Although previous work in this crustal block is limited, a single detrital thermochronology dataset (Espurt et al., 2018; sample 7) suggests a possible uplift phase around 30 Ma. Our results support this timing and provide the first direct thermochronological evidence of early Oligocene exhumation in the region derived from igneous bedrock.

D) Western Cordillera

Samples from the Western Cordillera yielded AFT ages of 29.8 Ma (IG22–05) and 23.5 Ma (IG22–04). While no U-Pb crystallization age is available for IG22–05 due to the presence of only inherited zircon components (~1 Ga), sample IG22–04 provides a more complete thermal history. Its zircon U-Pb age (29.7 ± 2 Ma) closely matches its AFT age (23.5 ± 3.6 Ma), suggesting rapid post-magmatic cooling, with emplacement and cooling occurring nearly simultaneously. Since both samples belong to the same crustal block, they likely record a shared tectono-thermal history, most plausibly reflecting post-magmatic thermal relaxation following magmatism.

This interpretation aligns well with results from Margirier et al. (2023), who studied the same crustal block slightly north of our study area (~3°S) and documented an early–middle Miocene post-magmatic cooling phase attributed to thermal relaxation after intrusion. Our results reinforce the idea that AFT thermochronology in this region primarily records cooling related to the final stages of magmatism rather than tectonic exhumation (Fig. 5A).

E) Amotape-Tahuin Block

The ATB is unconformably overlain by the Puyanco-Cazaderos and Cochurco series, indicating that the massif was at the surface during the Aptian to Coniacian or Santonian (Jaillard et al., 1999; Riel et al., 2014). Heating between ~80 and 45 Ma (Fig. 3) likely resulted from burial beneath Paleocene rocks, including the Gonzanama and Sacapalca formations (Hungerbühler et al., 2002; Jaillard et al., 1999), as there is no evidence of an increased geothermal gradient, such as volcanism, within the ATB during this period (Fig. 6). These findings align with a post–Late Cretaceous burial-related reheating phase previously documented by Espurt et al. (2018) in a Triassic granite of northern Peru. Following this, the ATB underwent heterogeneous cooling and exhumation.

The northernmost unit of the ATB, located north of the La Palma shear zone (Fig. 1B) experienced cooling between ~33 and 25 Ma at rates of ~30 °C/Ma. Spikings et al. (2005) reported an AFT and ZFT age of 61 and 68 Ma, respectively, in the same block, while Gabriele (2002)

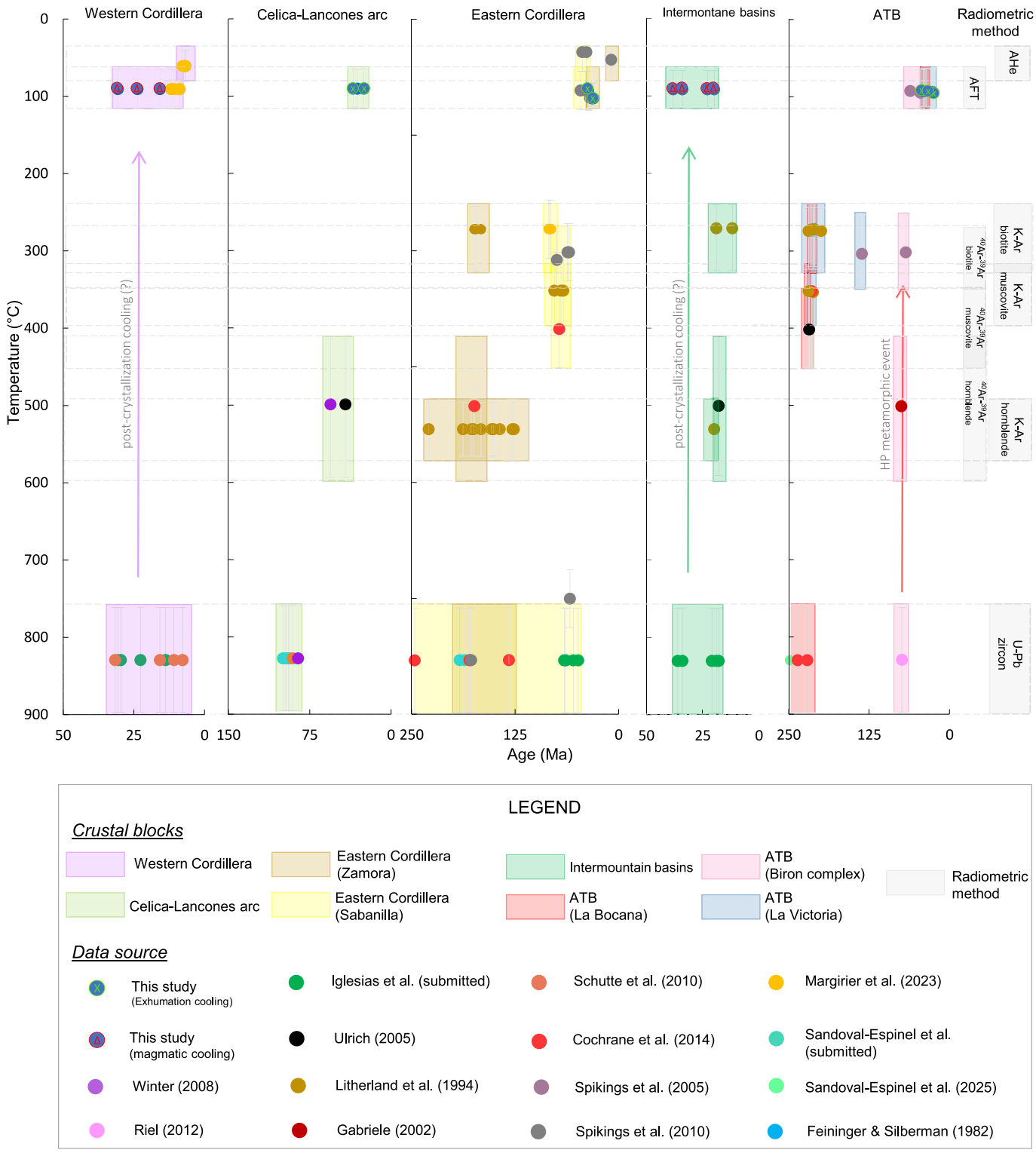

Fig. 6. Cooling temperature (°C) versus age (Ma) plots showing geochronological and thermochronological ages from bedrock rocks across different tectonostratigraphic units of southern Ecuador. Ages are from Cochrane et al. (2014), Feininger and Silberman (1982), Gabriele (2002), Iglesias et al. (2025), Litherland (1994), Margirier et al. (2023), Pratt et al. (2005), Riel et al. (2014), Sandoval-Espinel et al. (2025, submitted), Schütte et al. (2010), Spikings et al. (2001, 2005, 2010), Winter et al. (2010), and Urlich (2005).

obtained an age $^{40}Ar/^{39}Ar$ hornblende age of 75 ± 0.5 Ma. Documenting amphibolitized metagabbroic bodies in the area, Riel et al. (2014) attributed the ~75–73 Ma ages to high-temperature deformation. Their interpretation suggests either an accretion event or a poorly understood, localized tectonothermal event that might have partially overprinted pre-existing thermal and structural signatures. However, the AFT age of 61 ± 5 Ma and MTL of 12.4 ± 0.2 reported by Spikings et al. (2005) may not be directly linked to this slightly older high-temperature event. Spikings et al. (2005) noted that their AFT ages from the ATB generally do not correspond to specific, well-defined cooling events. Their ages

were interpreted as reflecting partially annealed fission tracks, suggesting that the samples experienced incomplete thermal resetting. This could explain the older apparent age despite the close spatial proximity to our sample. In contrast, the sample analyzed in this study likely records a more recent and distinct cooling episode, as indicated by its higher Chi-square (χ^2) probability value and longer MTL (13.5 μm; Table 2). The observed difference in AFT ages may therefore reflect localized thermal processes, such as hydrothermal activity, or structural influences, such as faulting. Additional data are required to better constrain these interpretations.

The *E*-W trending block of the ATB, located just south of the NZS, experienced a rapid cooling event between 45 and 40 Ma at rates of ~35 °C/Ma. This event is recorded in both the La Bocana Unit and the Triassic La Florida Pluton. Within the same block, Spikings et al. (2005) reported an AFT age of 38.8 ± 2.7 and MTL of 13.63 ± 0.19 μm, documenting the onset of cooling at ~43–39 Ma but at significantly lower rates of ~5.5–4.5 °C/Ma. The difference in cooling rates, despite similar AFT ages, is likely to be related to the constraints and assumptions used in the thermal modeling. Further south, the block comprising the La Victoria Unit (Fig. 1B) underwent cooling between ~33 and 25 Ma at rates of 30–35 °C/Ma.

5.2. *Cooling history of southern Ecuador and its relationship to Andean tectonic events*

The arrival of the Pallantanga Terrane at the northwestern margin of South America around 75–73 Ma (Cediel, 2019; Jaillard, 2022; Luzieux et al., 2006; Vallejo et al., 2019; Witt et al., 2023) marked the onset of cooling and exhumation in several regions along the northern Andes (i.e., Cediel and Shaw, 2019; Luzieux et al., 2006; Spikings et al., 2010; Witt et al., 2017). This event is thought to be recorded in southern Ecuador along the eastern margin of the Eastern Cordillera and the Sub-Andean Zone, within faulted blocks of the Zamora Batholith (Spikings et al., 2001, 2010). It also coincides with the deposition of the continental Tena Formation (72–57 Ma; Balkwill et al., 1995) in the Amazon foreland basin, which is interpreted as the first rocks sourced from the Eastern Cordillera, indicating that the Cordillera was uplifted during this period (Ruiz et al., 2004; Spikings et al., 2010). Prior to the Maastrichtian, rocks from the Amazon basin were derived from the Brazilian Shield (Martin-Gombojav and Winkler, 2008; Ruiz et al., 2004; Vallejo et al., 2021). However, our dataset does not record a Maastrichtian cooling signal. This absence may reflect the limited sampling of more easterly structural blocks, where such cooling has been proposed, or it may indicate that southern Ecuador does not preserve unequivocal evidence of this accretionary event documented farther north.

A reorientation of the Farallon plate convergence vector from NNE or NE to NE or ENE (~45–40 Ma; Fig. 5C; Jaillard, 2025; and references therein), significantly increased compression in the upper plate. This tectonic reorganization might have influenced the middle-late Eocene cooling event (~45–38 Ma), that we captured particularly on the western flank of the Eastern Cordillera (Sabanilla unit) and the core of the ATB (Fig. 7A). This event culminated with the deposition of unconformable conglomerates and volcanic rocks of late Eocene age, such as the Quingeo Formation (42–34 Ma; Hungerbühler et al., 2002; Jaillard, 2025; and references therein).

Subsequently, around 38 Ma, a slight increase in convergence rates (Fig. 5B; Maloney et al., 2013) likely contributed to the exhumation of the Celica Arc and the crustal block of Zamora Batholith bounded by the Nangaritza and Palanda faults (Fig. 7B). This event is evidenced by significant paleogeographic changes along the Ecuadorian margin and the northern Peruvian Andes, including widespread erosion and a shift from marine to terrestrial depositional environments (Espurt et al., 2018; Witt et al., 2019). This period has been interpreted as a major compressional event (Jaillard et al., 1995; Naeser et al., 1991). In southern Ecuador, late Eocene to early Oligocene compression has been specifically linked to a shift in lag-times (difference between the AFT and

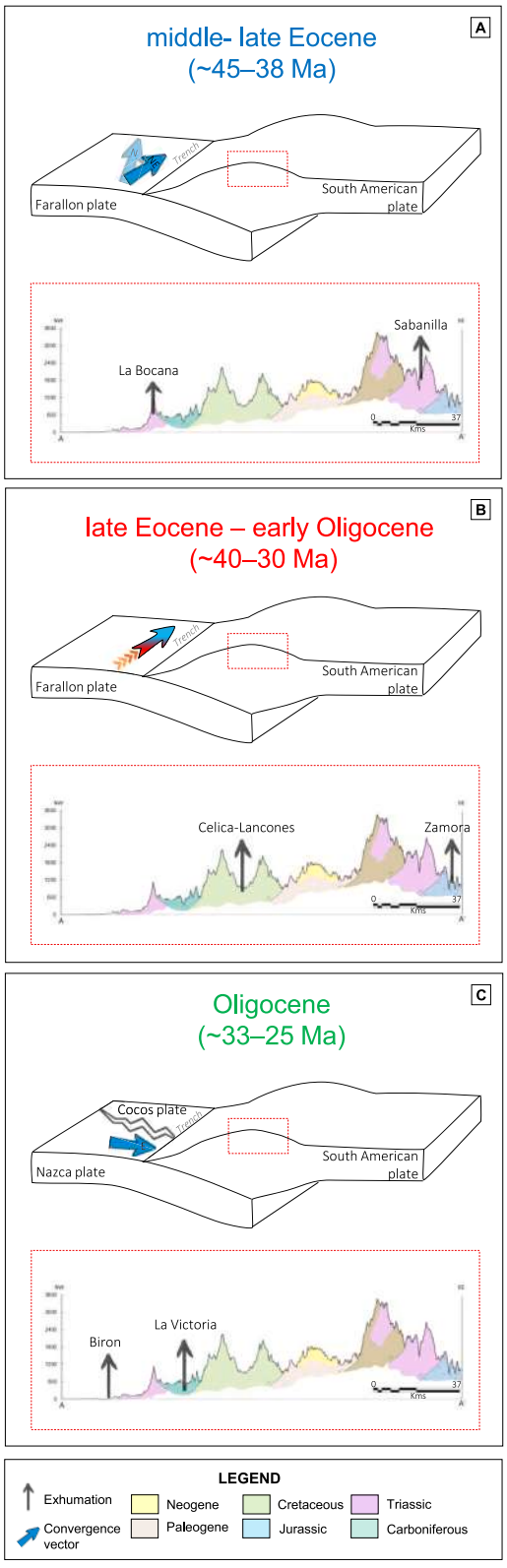

Fig. 7. Cartoon summary of major cooling intervals in southern Ecuador, showing the inferred causes for each interval and a profile of the study area (see Fig. 1 for location) indicating blocks that experienced cooling (upward-pointing arrows). (A) middle Eocene event illustrating a change in subduction vector direction. (B) late Eocene–Oligocene event depicting an increase in subduction rate. (C) late Oligocene–early Miocene event showing a renewed change in subduction vector direction.

the sedimentation age, see Malusà and Fitzgerald, 2020) recorded in the Tiyuyaku Formation of the Amazon foreland basin. Around ~36 Ma, lag times changed from relatively short values between ~50–36 Ma to progressively increasing lag times from ~36–30 Ma (see Ruiz, 2002; Spikings et al., 2010). This transition has been interpreted as reflecting a change in sediment provenance within the Eastern Cordillera. However, the results of this study indicate a decrease in exhumation rates, from higher cooling rates of ~20–35 °C/Ma during the middle- late Eocene (~45–38 Ma) to lower rates of ~15–30 °C/Ma during the late Eocene to early Oligocene (~40–30 Ma). Therefore, the observed increase in lag times may reflect slower exhumation rather than a shift in the sediment source region.

A tectonic plate rearrangement about 27–25 Ma, driven by the fragmentation of the Farallon Plate (Jaillard, 2025; Maloney et al., 2013) resulted in a shift in the subduction direction from ESE to E (Gordon and Jurdy, 1986; Pilger, 1984). This reconfiguration broadly coincides with the Oligocene (~33–25 Ma) exhumation event, which led to the exhumation of the peripheral blocks of the ATB in southern Ecuador (Fig. 7C). Furthermore, this event broadly coincides with a major arc magmatic flare-up event in Ecuador that occurred during the late Oligocene to early Miocene and was characterized by widespread ignimbrite eruptions and pluton emplacement (Schütte et al., 2010). Crustal thickening associated with magmatic addition can lead to surface uplift through isostatic compensation (see Farner and Lee, 2017). Additionally, magmatism can drive uplift through several mechanisms, including diapirism and crustal inflation associated with pluton emplacement, as well as decompression melting and magma generation triggered by basal lithospheric removal. For example, Perkins et al. (2016) documented crustal thickening and uplift in the Central Andes caused by the accumulation of buoyant magmatic bodies. While, Studies by Coldwell et al. (2011) and Garzione et al. (2006) in central Peru and Bolivia, respectively, have shown that removal of the lower continental crust and mantle lithosphere (via subduction erosion and delamination) induced asthenospheric upwelling, decompression melting, significant magmatic activity and ultimately surface uplift. The relative contributions of magmatism and tectonic processes to uplift in the southern Ecuadorian Andes remain poorly constrained, largely due to uncertainties in the volume and spatial distribution of the intrusive and volcanic material produced during the flare-up event.

5.3. *Heterogeneous uplift and topographic development of southern Ecuador*

Results from this study indicate that exhumation in southern Ecuador was already active by at least the middle Eocene. Although our thermochronological dataset (AFT ages) constrains cooling rather than absolute surface uplift, the integration of stratigraphic evidence (Hungerbühler et al., 2002; Jaillard et al., 1999; Steinmann et al., 1999) supports a heterogeneous pattern of topographic development across the region.

By the middle Miocene, large shallow-marine embayment (e.g., Loja) developed under extensional conditions and it is believed that it experienced marine incursions from the subsiding forearc (Progreso Basin; Steinmann et al., 1999). These processes led to the accumulation of coastal to shallow-marine facies between ~15 and 10 Ma within the southern intermontane basins. Stratigraphic evidence suggests that these coastal-marine systems were mainly supplied with detritus derived from the Eastern Cordillera and surrounding older volcanic formations (Hungerbühler et al., 2002; Steinmann et al., 1999), probably including material from the Celica–Lancones Basin, which is dominated by continental and volcaniclastic successions. The absence of middle Miocene marine deposits in the Celica–Lancones Basin (Jaillard et al., 1999) further supports the interpretation that both the Eastern Cordillera and the Celica–Lancones domain were already partially uplifted by this time. These structural highs likely formed the topographic margins of what is referred to the Miocene Loja embayment.

A regionally extensive angular unconformity dated between ~10 and 8 Ma across the intermontane marine basins (Hungerbühler et al., 2002) marks the onset of basin inversion and continental sedimentation, reflecting a major phase of uplift (Hungerbühler et al., 2002; Steinmann et al., 1999). Exhumation events younger than ~10 Ma enhanced topographic growth, through renewed compressional deformation, crustal shortening and erosion (Steinmann et al., 1999). These processes uplifted the 15–10 Ma shallow-marine deposits to their present elevations of ~2700 m. This evolution is consistent with regional evidence indicating that the main phase of Andean topographic development occurred during the Miocene (e.g., Anderson et al., 2016; Echeverri et al., 2015; Giambiagi et al., 2022; Howlett et al., 2025; Mosolf et al., 2011). None of our AFT ages or related modeling indicates cooling after 25 Ma, although the processes described above may correspond to the most significant phase of topographic development in the Ecuadorian Andes and could, in principle, have resulted in rocks crossing the AFT closure isotherm. An important implication is that the preservation of marine sedimentation suggests that incipient denudation occurred during uplift, or that denudation rates differed markedly between the marine basins and adjacent areas where sedimentation was either not preserved or may never have accumulated. Other possibilities should be considered: 1) net surface uplift without exhumation, in which topography increases without rocks being exhumed through isotherms (i.e., isotherms are uplifted together with the crust); 2) rocks were already at lower temperatures than the AFT partial annealing zone, so that the AFT system remained unreset throughout uplift prior to the last major phase of late Miocene uplift; and 3) a less likely scenario in which sedimentation balanced rock uplift, leaving the thermal structure essentially unchanged. A more quantitative assessment of uplift magnitude, rates, and spatial variability in this segment of the Andes will require future work. Such efforts should expand the AFT dataset and integrate apatite (U-Th)/He thermochronology, cosmogenic-nuclide analyses, and both thermokinematic and landscape-evolution modeling.

6. Conclusions

Apatite fission-track thermal modeling from southern Ecuador reveals a pattern of continuous cooling from the middle Eocene to the present, punctuated by three distinguishable cooling–exhumation intervals: ~45–38 Ma (middle Eocene), ~40–30 Ma (late Eocene to Oligocene), and ~ 33–25 Ma (late Oligocene to early Miocene). Two of these exhumation phases (~45–38 Ma and ~ 33–25 Ma) broadly coincide with documented changes in the direction of Nazca–South America plate convergence, whereas the ~40–30 Ma interval overlaps with an increase in convergence rate (Maloney et al., 2013).

Exhumation was spatially heterogeneous and varied across distinct crustal blocks. In the Eastern Cordillera, the Jurassic Zamora Batholith cooled during the late Eocene–Oligocene, whereas the adjacent Triassic Sabanilla Unit (structurally separated by the Palanda Fault) experienced earlier, middle-Eocene exhumation. A similar pattern characterizes the Amotape–Tahuin Block, where the core cooled during the middle Eocene, followed by younger late Oligocene–early Miocene exhumation in the fault-bounded peripheral domains. These observations indicate that reactivation of pre-existing faults modulated exhumation, accommodating deformation during regional tectonic reorganization. Finally, the temporal overlap between the late Oligocene–early Miocene exhumation phase and a proposed magmatic flare-up (Schütte et al., 2010) suggests that magmatism may have contributed to exhumation. The last major late Miocene uplift is not recorded in our AFT dataset. Preservation of marine sedimentation suggests limited or spatially variable denudation. This absence of cooling may reflect surface uplift without exhumation, prior cooling of rocks below the AFT partial annealing zone, or less-likely sedimentation balancing uplift. Together, these results indicate a dual influence of external plate-convergence dynamics and internal processes (magmatism and fault-driven block accommodation) in shaping the exhumation history of this segment of the Andes,

resulting is spatial variable exhumation patterns.

Supplementary data to this article can be found online at https://doi.org/10.1016/j.tecto.2026.231086.

CRediT authorship contribution statement

Leidy Carolina Sandoval Espinel: Writing – original draft, Visualization, Methodology, Formal analysis, Data curation. **Massimiliano Zattin:** Writing – review & editing, Supervision, Investigation, Formal analysis. **Mauricio A. Bermúdez:** Writing – review & editing, Supervision, Formal analysis. **Cesar Witt:** Writing – review & editing, Supervision, Formal analysis. **Jorge Iglesias:** Writing – review & editing, Methodology. **Maria Jose Hernández:** Writing – review & editing.

Funding sources

This work was supported by the PhD scholarship awarded to Sandoval-Espinel by the University of Padova (Grand: 2077712).

Declaration of competing interest

The authors declare that they have no known competing financial interests or personal relationships that could have appeared to influence the work reported in this paper.

Acknowledgments

We would like to thank Silvia Catto, Xiaoqin Jiao, Andrés Alarcón, and John Sandoval for their assistance in sample preparation for AFT and training in the AFT method. Additionally, Bermúdez, M. acknowledges the support of the Minciencias and ANH-Colombia thought the project 110993194496 (Contract: 80470-038-2023). We thank Jeff Apple Benowitz, Etienne Jaillard, and two anonymous reviewers for their thorough and helpful reviews, which substantially improved this manuscript. We also thank the editor, Samuel Angiboust, for his careful handling of the manuscript and valuable editorial guidance.

Data availability

Data will be made available on request.

References

Aizprua, C., Witt, C., Johansen, S.E., Barba, D., 2019. Cenozoic stages of forearc evolution following the accretion of a sliver from the Late Cretaceous-Caribbean large igneous province: SW Ecuador-NW Peru, 38 (4), 1441–1465. https://doi.org/10.1029/2018TC005235.

Anderson, V.J., Horton, B.K., Saylor, J.E., Mora, A., Tesón, E., Breecker, D.O., Ketcham, R.A., 2016. Andean topographic growth and basement uplift in southern Colombia: implications for the evolution of the Magdalena, Orinoco, and Amazon river systems. Geosphere 12 (4), 1235–1256. https://doi.org/10.1130/GES01294.1%J Geosphere.

Angulo-Romero, E., Beate, B., Romero-Cóndor, C., 2023. Zonificación del gradiente geotérmico en la cuenca Oriente de Ecuador a partir de temperatura de fondo de pozos. Bol. Geol. 45 (1), 119–139. https://doi.org/10.18273/revbol.v45n1-2023006.

Armstrong, P.A., Ehlers, T.A., Chapman, D.S., Farley, K.A., Kamp, P.J.J., 2003. Exhumation of the Central Wasatch Mountains, Utah: 1. Patterns and timing of exhumation deduced from low-temperature thermochronology data. J. Geophys. Res. Solid Earth 108 (B3). https://doi.org/10.1029/2001JB001708.

Baby, P., Rivadeneira, M., Barragán, R., Christophoul, F., 2013. Thick-skinned tectonics in the Oriente foreland basin of Ecuador. Geol. Soc. Lond. Spec. Publ. 377 (1), 59–76. https://doi.org/10.1144/SP377.1.

Balkwill, H., Rodrigue, G., Paredes, F., Almeida, J., 1995. Northern part of Oriente Basin, Ecuador: reflection seismic expression of structures. In: Petroleum Basins of South America.

Barbarand, J., Hurford, T., Carter, A., 2003. Variation in apatite fission-track length measurement: implications for thermal history modelling. Chem. Geol. 198 (1), 77–106. https://doi.org/10.1016/S0009-2541(02)00423-0.

Bermúdez, M.A., van der Beek, P., Bernet, M., 2011. Asynchronous Miocene–Pliocene exhumation of the central Venezuelan Andes. Geology 39 (2), 139–142. https://doi.org/10.1130/G31582.1.

Bermúdez, M.A., Bernet, M., Kohn, B.P., Brichau, S., 2019. Exhumation-Denudation history of the Maracaibo Block, Northwestern South America: insights from thermochronology. In: Cediel, F., Shaw, R.P. (Eds.), Geology and Tectonics of Northwestern South America: The Pacific-Caribbean-Andean Junction (pp. 879–898). Springer International Publishing. https://doi.org/10.1007/978-3-319-76132-9_13.

Boschman, L.M., 2021. Andean mountain building since the late cretaceous: a paleoelevation reconstruction. Earth Sci. Rev. 220, 103640. https://doi.org/10.1016/j.earscirev.2021.103640.

Brandon, M.T., Roden-Tice, M.K., Garver, J.I., 1998. Late Cenozoic exhumation of the Cascadia accretionary wedge in the Olympic Mountains, Northwest Washington State. Geol. Soc. Am. Bull. 110, 985–1009.

Brichau, S., Reyes, P., Gautheron, C., Hernández, M.J., Michaud, F., Leisen, M., O'Sullivan, P., 2021. First timing constraints on the Ecuadorian Coastal Cordillera exhumation: geodynamic implications. J. S. Am. Earth Sci. 105, 103007. https://doi.org/10.1016/j.jsames.2020.103007.

Carlson, W.D., Donelick, R.A., Ketcham, R.A., 1999. Variability of apatite fission-track annealing kinetics: I. Experimental results. Am. Mineral. 84 (9), 1213–1223. https://doi.org/10.2138/am-1999-0901.

Cediel, F., 2019. Phanerozoic orogens of Northwestern South America: cordilleran-type orogens. Taphrogenic tectonics. The Maracaibo orogenic float. The Chocó-Panamá indenter. In: Cediel, F., Shaw, R.P. (Eds.), Geology and Tectonics of Northwestern South America: The Pacific-Caribbean-Andean Junction (pp. 3–95). Springer International Publishing. https://doi.org/10.1007/978-3-319-76132-9_1.

Cediel, F., Shaw, R.P., 2019. Geology and Tectonics of Northwestern South America: The Pacific-Caribbean-Andean Junction. Springer.

Cochrane, R., Spikings, R., Gerdes, A., Ulianov, A., Mora, A., Villagómez, D., Chiaradia, M., 2014. Permo-Triassic anatexis, continental rifting and the disassembly of western Pangaea. Lithos 190-191, 383–402. https://doi.org/10.1016/j.lithos.2013.12.020.

Coldwell, B., Clemens, J., Petford, N., 2011. Deep crustal melting in the Peruvian Andes: felsic magma generation during delamination and uplift. Lithos 125 (1), 272–286. https://doi.org/10.1016/j.lithos.2011.02.011.

Donelick, R.A., O'Sullivan, P.B., Ketcham, R.A., 2005. Apatite fission-track analysis. Rev. Mineral. Geochem. 58 (1), 49–94. https://doi.org/10.2138/rmg.2005.58.3.

Echeverri, S., Cardona, A., Pardo, A., Monsalve, G., Valencia, V.A., Borrero, C., López, S., 2015. Regional provenance from southwestern Colombia fore-arc and intra-arc basins: implications for middle to late Miocene orogeny in the Northern Andes. Terra Nova 27 (5), 356–363. https://doi.org/10.1111/ter.12167.

Eguez, A., Alvarado, A., Yepes, H., Machette, M.N., Costa, C., Dart, R.L., Bradley, L., 2003. Database and map of quaternary faults and folds of Ecuador and its offshore regions. In: US Geological Survey Open-File Report, 3, p. 289.

Ehlers, T., Chaudhri, T., Kumar, S., Fuller, C., Willet, S., Ketcham, R.A., Fu, F.Q., 2005. Computational tools for low-temperature thermochronometer interpretation. In: Reiners, P., Ehlers, T. (Eds.), Low-Temperature Thermochronology: Techniques, Interpretations, Applications: Reviews in Mineralogy and Geochemistry: Chantilly, VA. Mineralogical Society of America, Geochemical Society, pp. 589–622.

Espurt, N., Brusset, S., Baby, P., Henry, P., Vega, M., Calderon, Y., Saillard, M., 2018. Deciphering the late cretaceous-Cenozoic structural evolution of the North Peruvian forearc system. Tectonics 37 (1), 251–282. https://doi.org/10.1002/2017tc004536.

Farner, M.J., Lee, C.-T.A., 2017. Effects of crustal thickness on magmatic differentiation in subduction zone volcanism: a global study. Earth Planet. Sci. Lett. 470, 96–107. https://doi.org/10.1016/j.epsl.2017.04.025.

Feininger, T., Silberman, M.L., 1982. *K-Ar geochronology of basement rocks on the northern flank of the Huancabama deflection, Ecuador* [Report](82-206) (Open-File Report, Issue. U. S. G. Survey. https://pubs.usgs.gov/publication/ofr82206.

Gabriele, P., 2002. HP Terranes Exhumation in an Active Margin Setting: Geology, Petrology and Geochemistry of the Raspas Complex in SW Ecuador Univ. of Lausanne.

Gallagher, K., Brown, R., Johnson, C., 1998. Fission track analysis and its applications to geological problems. Annu. Rev. Earth Planet. Sci. 26 (1), 519–572.

Garzione, C.N., Molnar, P., Libarkin, J.C., MacFadden, B.J., 2006. Rapid late Miocene rise of the Bolivian Altiplano: evidence for removal of mantle lithosphere. Earth Planet. Sci. Lett. 241 (3), 543–556. https://doi.org/10.1016/j.epsl.2005.11.026.

George, S.W.M., Horton, B.K., Vallejo, C., Jackson, L.J., Gutierrez, E.G., 2021. Did accretion of the Caribbean oceanic plateau drive rapid crustal thickening in the northern Andes? Geology 49 (8), 936–940. https://doi.org/10.1130/g48509.1.

George, S.W.M., Perez, N.D., Struble, W., Curry, M.E., Horton, B.K., 2022. Aseismic ridge subduction focused late Cenozoic exhumation above the Peruvian flat slab. Earth Planet. Sci. Lett. 600, 117754. https://doi.org/10.1016/j.epsl.2022.117754.

Giambiagi, L., Tassara, A., Echaurren, A., Julve, J., Quiroga, R., Barrionuevo, M., Lothari, L., 2022. Crustal anatomy and evolution of a subduction-related orogenic system: Insights from the Southern Central Andes (22-35°S). Earth Sci. Rev. 232, 104138. https://doi.org/10.1016/j.earscirev.2022.104138.

Gleadow, A.J.W., 1981. Fission-track dating methods: what are the real alternatives? Nucl. Tracks. 5 (1), 3–14. https://doi.org/10.1016/0191-278X(81)90021-4.

Gleadow, A.J.W., Kohn, B.P., Brown, R.W., O'Sullivan, P.B., Raza, A., 2002. Fission track thermotectonic imaging of the Australian continent. Tectonophysics 349 (1), 5–21. https://doi.org/10.1016/S0040-1951(02)00043-4.

Gordon, R.G., Jurdy, D.M., 1986. Cenozoic global plate motions. J. Geophys. Res. Solid Earth 91 (B12), 12389–12406. https://doi.org/10.1029/JB091iB12p12389.

Gutscher, M.-A., 2002. Andean subduction styles and their effect on thermal structure and interplate coupling. J. S. Am. Earth Sci. 15 (1), 3–10. https://doi.org/10.1016/S0895-9811(02)00002-0.

Gutscher, M.-A., Spakman, W., Bijwaard, H., Engdahl, E.R., 2000. Geodynamics of flat subduction: Seismicity and tomographic constraints from the Andean margin. Tectonics 19 (5), 814–833. https://doi.org/10.1029/1999TC001152.
Hernández, M.J., Michaud, F., Collot, J.-Y., d'Acremont, E., Proust, J.-N., Barba, D., 2024. Evolution of the Manabí forearc basin in Ecuador: from the collision of Caribbean oceanic plateau to the build up of the Andes and Coastal Cordilleras. Tectonophysics 870, 230133. https://doi.org/10.1016/j.tecto.2023.230133.
Horton, B.K., 2018. Sedimentary record of Andean mountain building. Earth Sci. Rev. 178, 279–309. https://doi.org/10.1016/j.earscirev.2017.11.025.
Horton, B.K., Parra, M., Mora, A., 2020. Construction of the Eastern Cordillera of Colombia: insights from the sedimentary record. In: Gómez, J.M.Z. (Ed.), The Geology of Colombia, 3, pp. 67–88. https://doi.org/10.32685/pub.esp.37.2019.03.
Howlett, C.J., Ronemus, C.B., Carrapa, B., DeCelles, P.G., 2025. Miocene construction of the high andes recorded by exhumation of the frontal cordillera, La Ramada Massif of Western Argentina (32°S). Tectonics 44 (1), e2024TC008433. https://doi.org/10.1029/2024TC008433.
Hughes, R.A., Pilatasig, L.F., 2002. Cretaceous and Tertiare terrane accretion in the Cordillera occidental of the Andes of Ecuador. Tectonophysics 345, 29–48.
Hungerbühler, D., Steinmann, M., Winkler, W., Seward, D., Egüez, A., Peterson, D.E., Hammer, C., 2002. Neogene stratigraphy and Andean geodynamics of southern Ecuador. Earth Sci. Rev. 57 (1), 75–124. https://doi.org/10.1016/S0012-8252(01)00071-X.
Hurford, A.J., Green, P.F., 1983. The zeta age calibration of fission-track dating. Chem. Geol. 41, 285–317. https://doi.org/10.1016/S0009-2541(83)80026-6.
Iglesias, J., Witt, C., Sandoval-Espinel, L.C., Zattin, M., Poujol, M., Bruguier, O., Poma, O., Hernandez, M.J., Seyler, M., Bosch, D., Chanier, F., Ventalon, S., Liorzou, C., 2025. Petrogenesis and Tectonic Evolution of Cenozoic Magmatism in the Southernmost Northern Andes: Insights from Zircon. Petrochronology (Under review, Gcubed).
Jaillard, E., 2022. Late Cretaceous-Paleogene orogenic build-up of the Ecuadorian Andes: review and discussion. Earth Sci. Rev. 230. https://doi.org/10.1016/j.earscirev.2022.104033.
Jaillard, E., 2025. Did the evolution from oblique to normal convergence contribute to the Andean building? J. S. Am. Earth Sci. 152, 105312. https://doi.org/10.1016/j.jsames.2024.105312.
Jaillard, E., Sempere, T., Soler, P., Carlier, G., Marocco, R., 1995. The role of Tethys in the evolution of the Northern Andes between late Permian and late Eocene times. In: Nairn, A.E.M., Ricou, L.-E., Vrielynck, B., Dercourt, J. (Eds.), The Tethys Ocean. Springer, US, pp. 463–492. https://doi.org/10.1007/978-1-4899-1558-0_15.
Jaillard, E., Ordoñez, M., Berrones, G., Bengtson, P., Bonhomme, M., Jimenez, N., Zambrano, I., 1996. Sedimentary and tectonic evolution of the arc zone of Southwestern Ecuador during late cretaceous and early Tertiary times. J. S. Am. Earth Sci. 9 (1), 131–140. https://doi.org/10.1016/0895-9811(96)00033-8.
Jaillard, E., Laubacher, G., Bengtson, P., Dhondt, A.V., Bulot, L., 1999. Stratigraphy and evolution of the cretaceous forearc Celica-Lancones basin of southwestern Ecuador. J. S. Am. Earth Sci. 12, 51–68.
Jaillard, E., Bengtson, P., Dhondt, A.V., 2005. Late cretaceous marine transgressions in Ecuador and northern Peru: a refined stratigraphic framework. J. S. Am. Earth Sci. 19 (3), 307–323. https://doi.org/10.1016/j.jsames.2005.01.006.
Kennan, L., 2000. Large-scale geomorphology in the Central Andes of Peru and Bolivia: relation to tectonic, magmatic and climatic processes. Geomorphol. Glob. Tecton. 167–192.
Kerr, A.C., Tarney, J., 2005. Tectonic evolution of the Caribbean and northwestern South America: the case for accretion of two late cretaceous oceanic plateaus. Geology 33 (4). https://doi.org/10.1130/g21109.1.
Ketcham, R.A., 2005. Forward and inverse modeling of low-temperature thermochronometry data. Rev. Mineral. Geochem. 58 (1), 275–314. https://doi.org/10.2138/rmg.2005.58.11.
Ketcham, R.A., Carter, A., Donelick, R.A., Barbarand, J., Hurford, A.J., 2007. Improved modeling of fission-track annealing in apatite. Am. Mineral. 92 (5–6), 799–810. https://doi.org/10.2138/am.2007.2281.
Litherland, M., 1994. The metamorphic belts of Ecuador. Overseas Mem. 11, 1–147.
Luzieux, L.D.A., Heller, F., Spikings, R., Vallejo, C.F., Winkler, W., 2006. Origin and cretaceous tectonic history of the coastal Ecuadorian forearc between 1°N and 3°S: paleomagnetic, radiometric and fossil evidence. Earth Planet. Sci. Lett. 249 (3), 400–414. https://doi.org/10.1016/j.epsl.2006.07.008.
Maloney, K.T., Clarke, G.L., Klepeis, K.A., Quevedo, L., 2013. The late Jurassic to present evolution of the Andean margin: drivers and the geological record. Tectonics 32 (5), 1049–1065. https://doi.org/10.1002/tect.20067.
Malusà, M.G., Fitzgerald, P.G., 2019. From cooling to exhumation: setting the reference frame for the interpretation of thermochronologic data. In: Malusà, M.G., Fitzgerald, P.G. (Eds.), Fission-Track Thermochronology and its Application to Geology. Springer International Publishing, pp. 147–164. https://doi.org/10.1007/978-3-319-89421-8_8.
Malusà, M.G., Fitzgerald, P.G., 2020. The geologic interpretation of the detrital thermochronology record within a stratigraphic framework, with examples from the European Alps, Taiwan and the Himalayas. Earth Sci. Rev. 201, 103074. https://doi.org/10.1016/j.earscirev.2019.103074.
Margirier, A., Strecker, M.R., Reiners, P.W., Thomson, S.N., Casado, I., George, S.W.M., Alvarado, A., 2023. Late Miocene exhumation of the Western Cordillera, Ecuador, driven by increased coupling between the subducting Carnegie Ridge and the south American Continent. Tectonics 42 (1), e2022TC007344. https://doi.org/10.1029/2022TC007344.
Martin-Gombojav, N., Winkler, W., 2008. Recycling of Proterozoic crust in the Andean Amazon foreland of Ecuador: implications for orogenic development of the Northern Andes. Terra Nova 20 (1), 22–31. https://doi.org/10.1111/j.1365-3121.2007.00782.x.
Michaud, F., Witt, C., Royer, J.-Y., 2009. Influence of the subduction of the Carnegie volcanic ridge on Ecuadorian geology: reality and fiction. In: Kay, S.M., Ramos, V.A., Dickinson, W.R. (Eds.), Backbone of the Americas: Shallow Subduction, Plateau Uplift, and Ridge and Terrane Collision. Geological Society of America, p. 0. https://doi.org/10.1130/2009.1204(10).
Mora, A., Horton, B.K., Mesa, A., Rubiano, J., Ketcham, R.A., Parra, M., Stockli, D.F., 2010. Migration of Cenozoic deformation in the Eastern Cordillera of Colombia interpreted from fission track results and structural relationships: implications for petroleum systems. AAPG Bull. 94 (10), 1543–1580. https://doi.org/10.1306/01051009111.
Mosolf, J.G., Horton, B.K., Heizler, M.T., Matos, R., 2011. Unroofing the core of the central Andean fold-thrust belt during focused late Miocene exhumation: evidence from the Tipuani-Mapiri wedge-top basin, Bolivia. Basin Res. 23 (3), 346–360. https://doi.org/10.1111/j.1365-2117.2010.00491.x.
Mourier, T., 1988. Transición entre Andes Marginales y Andes Cordilleranos: Evolución Sedimentaria, Magmática y Estructural Deflexión de Huancabamba: 3° a 8° Lat. S; Norte del Perú y Sur de Ecuador. Universidad de Paris Sur.
Naeser, C.W., Crochet, J.Y., Jaillard, E., Laubacher, G., Mourier, T., Sige, B., 1991. Tertiary fission-track ages from the Bagua syncline (northern Peru): Stratigraphic and tectonic implications. J. S. Am. Earth Sci. 4, 61–71.
Noble, S.R., Aspden, J.A., Jemielita, R., 1997. Northern Andean crustal evolution: new U-Pb geochronological constraints from Ecuador. GSA Bull. 109 (7), 789–798. https://doi.org/10.1130/0016-7606(1997)109<0789:NACENU>2.3.CO;2.
Noriega-Londoño, S., Restrepo-Moreno, S.A., Vinasco, C., Bermúdez, M.A., Min, K., 2020. Thermochronologic and geomorphometric constraints on the Cenozoic landscape evolution of the Northern Andes: Northwestern Central Cordillera, Colombia. Geomorphology 351, 106890. https://doi.org/10.1016/j.geomorph.2019.106890.
Perkins, J.P., Ward, K.M., de Silva, S.L., Zandt, G., Beck, S.L., Finnegan, N.J., 2016. Surface uplift in the Central Andes driven by growth of the altiplano puna magma body. Nat. Commun. 7 (1), 13185. https://doi.org/10.1038/ncomms13185.
Pilger, R.H., 1984. Cenozoic plate kinematics, subduction and magmatism: South American Andes. J. Geol. Soc. Lond. 141 (5), 793–802.
Pratt, W.T., Duque, P., Ponce, M., 2005. An autochthonous geological model for the eastern Andes of Ecuador. Tectonophysics 399 (1), 251–278. https://doi.org/10.1016/j.tecto.2004.12.025.
Restrepo-Moreno, S.A., Foster, D.A., Bernet, M., Min, K., Noriega, S., 2019. Morphotectonic and Orogenic Development of the Northern Andes of Colombia: A Low-Temperature Thermochronology Perspective. In: Cediel, F., Shaw, R.P. (Eds.), Geology and Tectonics of Northwestern South America: The Pacific-Caribbean-Andean Junction. Springer International Publishing, pp. 749–832. https://doi.org/10.1007/978-3-319-76132-9_11.
Reynaud, C., Lapierre, H., Jaillard, E., Benítez, S., Berrones, G., Mascle, G., 1996. Mineralogical and Geochemical Characterization of Middle Cretaceous to Paleocene Oceanic and Continental Volcanic Rocks from Southwestern Ecuador.
Reynaud, C., Jaillard, É., Lapierre, H., Mamberti, M., Mascle, G.H., 1999. Oceanic plateau and island arcs of southwestern Ecuador: their place in the geodynamic evolution of northwestern South America. Tectonophysics 307 (3), 235–254. https://doi.org/10.1016/S0040-1951(99)00099-2.
Riel, N., Martelat, J.-E., Guillot, S., Jaillard, E., Monié, P., Yuquilema, J., Mercier, J., 2014. Fore arc tectonothermal evolution of the El Oro metamorphic province (Ecuador) during the Mesozoic. Tectonics 33 (10), 1989–2012. https://doi.org/10.1002/2014TC003618.
Ronda, G., Ghiglione, M.C., Martinod, J., Barberón, V., Ramos, M.E., Coutand, I., Kislitsyn, R., 2022. Early cretaceous to Cenozoic growth of the Patagonian Andes as revealed by low-temperature thermochronology. Tectonics 41 (10), e2021TC007113. https://doi.org/10.1029/2021TC007113.
Ruiz, G.M.H., 2002. Exhumation of the Northern Sub-Andean Zone of Ecuador and its Source Regions: A Combined Thermochronological and Heavy Mineral Approach ETH Zurich.
Ruiz, G.M.H., Seward, D., Winkler, W., 2004. Detrital thermochronology – a new perspective on hinterland tectonics, an example from the Andean Amazon Basin, Ecuador. Basin Res. 16 (3), 413–430. https://doi.org/10.1111/j.1365-2117.2004.00239.x.
Sandoval Espinel, L.C., Witt, C., Iglesias, J., Zattin, M., Bruguier, O., Poujol, M., Sandoval Espinel, J.J., 2026. Mesozoic magmatism in the Andes of southern Ecuador and northern Peru: tectonic insights from whole-rock chemistry and zircon petrochronology. Lithos 522-523, 108389. https://doi.org/10.1016/j.lithos.2025.108389.
Sandoval-Espinel, J.J., Sandoval-Espinel, L.C., Bermúdez, M.A., Bernet, M., Kohn, B., Amaya, S., Zuluaga, C., 2024. Thermal and burial history of the axial Arcabuco-Floresta segment, Eastern Cordillera basin, Colombia: evidence from low-temperature thermochronology and numerical modelling [original research]. Front. Earth Sci. 12. https://doi.org/10.3389/feart.2024.1471172.
Sandoval-Espinel, L.C., Witt, C., Zattin, M., Poujol, M., Bruguier, O., Chiaradia, M., Bermudez, M., 2025. Pervasive crustal reworking along the proto-Andean margin of northern Peru and southern Ecuador: Insights from U-Pb, geochemical, and isotopic analyses of zircon. J. S. Am. Earth Sci. 158, 105502. https://doi.org/10.1016/j.jsames.2025.105502.
Schütte, P., Chiaradia, M., Beate, B., 2010. Geodynamic controls on Tertiary arc magmatism in Ecuador: constraints from U–Pb zircon geochronology of Oligocene–Miocene intrusions and regional age distribution trends. Tectonophysics 489 (1–4), 159–176. https://doi.org/10.1016/j.tecto.2010.04.015.
Spikings, R.A., Seward, D., Winkler, W., Ruiz, G.M., 2000. Low-temperature thermochronology of the northern Cordillera real, Ecuador: tectonic insights from

zircon and apatite fission track analysis. Tectonics 19 (4), 649–668. https://doi.org/10.1029/2000tc900010.

Spikings, R.A., Winkler, W., Seward, D., Handler, R., 2001. Along-strike variations in the thermal and tectonic response of the continental Ecuadorian Andes to the collision with heterogeneous oceanic crust. Earth Planet. Sci. Lett. 186 (1), 57–73. https://doi.org/10.1016/S0012-821X(01)00225-4.

Spikings, R.A., Winkler, W., Hughes, R.A., Handler, R., 2005. Thermochronology of allochthonous terranes in Ecuador: unravelling the accretionary and post-accretionary history of the Northern Andes. Tectonophysics 399 (1–4), 195–220. https://doi.org/10.1016/j.tecto.2004.12.023.

Spikings, R.A., Crowhurst, P.V., Winkler, W., Villagomez, D., 2010. Syn- and post-accretionary cooling history of the Ecuadorian Andes constrained by their in-situ and detrital thermochronometric record. J. S. Am. Earth Sci. 30 (3), 121–133. https://doi.org/10.1016/j.jsames.2010.04.002.

Steinmann, M., Hungerbühler, D., Seward, D., Winkler, W., 1999. Neogene tectonic evolution and exhumation of the southern Ecuadorian Andes: a combined stratigraphy and fission-track approach. Tectonophysics 307 (3), 255–276. https://doi.org/10.1016/S0040-1951(99)00100-6.

Urlich, T., 2005. Summary Report on Ar/Ar Dating for MAP: GAC. *Activity PE–05 Peru.* Laboratory Pacific Centre for Isotopic Geochemical Research Earth Ocean Sciences. University of British Columbia, Vancouver.

Valarezo, M.E., Vallejo, C., Horton, B.K., Gaibor, J., Esteban, J., Jackson, L.J., Beate, B., 2019. Sedimentological and provenance analysis of the Río Playas stratigraphic section: implications for the evolution of the Alamor-Lancones Basin of southern Ecuador and northern Peru. J. S. Am. Earth Sci. 94. https://doi.org/10.1016/j.jsames.2019.102239.

Vallejo, C., Spikings, R.A., Luzieux, L., Winkler, W., Chew, D., Page, L., 2006. The early interaction between the Caribbean Plateau and the NW South American Plate. Terra Nova 18 (4), 264–269. https://doi.org/10.1111/j.1365-3121.2006.00688.x.

Vallejo, C., Spikings, R.A., Horton, B.K., Luzieux, L., Romero, C., Winkler, W., Thomsen, T.B., 2019. Chapter 8 - late cretaceous to miocene stratigraphy and provenance of the coastal forearc and Western Cordillera of Ecuador: evidence for accretion of a single oceanic plateau fragment. In: Horton, B.K., Folguera, A. (Eds.), Andean Tectonics. Elsevier, pp. 209–236. https://doi.org/10.1016/B978-0-12-816009-1.00010-1.

Vallejo, C., Romero, C., Horton, B.K., Spikings, R.A., Gaibor, J., Winkler, W., Mariño, E., 2021. Jurassic to early Paleogene sedimentation in the Amazon region of Ecuador: implications for the paleogeographic evolution of northwestern South America. Glob. Planet. Chang. 204, 103555. https://doi.org/10.1016/j.gloplacha.2021.103555.

Vermeesch, P., 2018. IsoplotR: a free and open toolbox for geochronology. Geosci. Front. 9 (5), 1479–1493. https://doi.org/10.1016/j.gsf.2018.04.001.

Winter, L.S., Tosdal, R.M., Mortensen, J.K., Franklin, J.M., 2010. Volcanic stratigraphy and geochronology of the cretaceous Lancones Basin, Northwestern Peru: position and timing of giant VMS deposits. Econ. Geol. 105 (4), 713–742. https://doi.org/10.2113/gsecongeo.105.4.713. %J Economic Geology.

Witt, C., Rivadeneira, M., Poujol, M., Barba, D., Beida, D., Beseme, G., Montenegro, G., 2017. Tracking ancient magmatism and Cenozoic topographic growth within the Northern Andes forearc: constraints from detrital U-Pb zircon ages. Geol. Soc. Am. Bull. 129 (3–4), 415–428. https://doi.org/10.1130/b31530.1.

Witt, C., Reynaud, J.Y., Barba, D., Poujol, M., Aizprua, C., Rivadeneira, M., Amberg, C., 2019. From accretion to forearc basin initiation: the case of SW Ecuador, Northern Andes. Sediment. Geol. 379, 138–157. https://doi.org/10.1016/j.sedgeo.2018.11.009.

Witt, C., Poujol, M., Chiaradia, M., Villagomez, D., Seyler, M., Averbuch, O., Bouden, N., 2023. Geodynamic controls in the southernmost Northern Andes magmatic arc: trace elements and Hf-O isotopic systematics in forearc detrital zircon. GSA Bull. https://doi.org/10.1130/b36510.1.

Zapata, S., Sobel, E.R., del Papa, C., Jelinek, A.R., Glodny, J., 2019. Using a paleosurface to constrain low-temperature thermochronological data: tectonic evolution of the Cuevas range, Central Andes. Tectonics 38 (11), 3939–3958. https://doi.org/10.1029/2019TC005887.